






The SOUX AGN sample: optical/UV/X-ray SEDs and the nature of the disc

Jake A. J. Mitchell ¹★, Chris Done ¹★, Martin J. Ward,¹ Daniel Kynoch ^{1,2,3}, Scott Hagen ¹,
Elisabeta Lusso ^{4,5} and Hermine Landt¹

¹Centre for Extragalactic Astronomy, Department of Physics, Durham University, South Road, Durham DH1 3LE, UK

²Astronomical Institute, Czech Academy of Sciences, Boční II 1401, CZ-141 00 Prague, Czech Republic

³School of Physics and Astronomy, University of Southampton, University Road, Southampton SO17 1BJ, UK

⁴Dipartimento di Fisica e Astronomia, Università di Firenze, via G. Sansone 1, I-50019 Sesto Fiorentino, Firenze, Italy

⁵INAF – Osservatorio Astrofisico di Arcetri, L.go Enrico Fermi 5, I-50125 Firenze, Italy

Accepted 2023 June 5. Received 2023 May 12; in original form 2022 October 21

ABSTRACT

We use the SOUX sample of ~ 700 active galactic nucleus (AGN) to form average optical-ultraviolet (UV)-X-rays spectral energy distributions (SEDs) on a two-dimensional (2D) grid of M_{BH} and L_{2500} . We compare these with the predictions of a new AGN SED model, QSOSED, which includes prescriptions for both hot and warm Comptonization regions as well as an outer standard disc. This predicts the overall SED fairly well for $7.5 < \log(M_{\text{BH}}/M_{\odot}) < 9.0$ over a wide range in L/L_{Edd} , but at higher masses the outer disc spectra in the model are far too cool to match the data. We create optical-UV composites from the entire Sloan Digital Sky Survey sample and use these to show that the mismatch is due to there being no significant change in spectral shape of the optical-UV continuum across several decades of M_{BH} at constant luminosity. We show for the first time that this cannot be matched by standard disc models with high black hole spin. These apparently fit, but are not self-consistent as they do not include the General Relativistic effects for the emission to reach the observer. At high spin, increased gravitational redshift compensates for almost all of the higher temperature emission from the smaller inner disc radii. The data do not match the predictions made by any current accretion flow model. Either the disc is completely covered by a warm Comptonization layer whose properties change systematically with L/L_{Edd} , or the accretion flow structure is fundamentally different to that of the standard disc models.

Key words: accretion, accretion discs – black hole physics – galaxies: active – galaxies: high-redshift – quasars: emission lines – quasars: supermassive black holes.

1 INTRODUCTION

Active galactic nuclei (AGNs) are powered by mass accretion on to a supermassive black hole (SMBH). They emit radiation over a large swathe of the electromagnetic spectrum. This emission is often represented in the form of a spectral energy distribution (SED), which shows the power emitted as a function of frequency. Therefore, SEDs can be used as a powerful diagnostic tool, allowing us to probe the physical structures and emission mechanisms in these objects. These show clearly that the AGN emission cannot be solely explained by a standard (Shakura & Sunyaev 1973) disc model. The reality is much more complex (see e.g. Lawrence 2012 and references therein).

AGN span a very wide range in mass (from 10^5 – $10^{10} M_{\odot}$) and luminosity, and display distinctly different SEDs across this parameter space. The effect of orientation along our line of sight with respect to an equatorial obscurer (i.e. the dusty torus) is at the core of the ‘unified model’ (Antonucci 1993). Nonetheless, whilst orientation is surely a key parameter, the systematic differences in SED shape, seen with changing mass and luminosity (e.g. Vasudevan & Fabian

2007; Jin et al. 2012; Lusso & Risaliti 2016a), strongly indicate an intrinsic change in the broad-band SED as a function of both mass and/or luminosity.

Intrinsic changes in the SED are well documented in black hole binary (BHB) systems (Done, Gierliński & Kubota 2007). There is a strong spectral transition which occurs at $\sim 0.02L_{\text{Edd}}$ as the source slowly dims down from a soft, thermal state to a hard, Comptonized state. These different emission mechanisms most likely signal a fundamental change in the nature of the accretion flow, from a geometrically thin, cool, optically thick disc similar to the standard disc models (Shakura & Sunyaev 1973) to an optically thin, hot, geometrically thick flow such as the advection-dominated accretion flow (ADAF) models (Narayan & Yi 1995).

A single model for AGN would then take this state transition in BHB and scale it to the higher mass SMBH. Indeed, a strong spectral change is seen in some AGN that vary across the transition luminosity of $\sim 0.02L_{\text{Edd}}$ (Krumpe et al. 2017; Noda & Done 2018; Ruan et al. 2019). These ‘changing-look’ AGN show hard X-ray spectra below a few per cent of Eddington which are dominated by the hard X-ray power law, similar to the hard state in BHB. However, above a few per cent of Eddington, i.e. when the BHB show pre-dominantly disc-dominated spectra, the AGN instead show spectra with a substantial amount of non-disc emission. This is shown

* E-mail: jake.a.mitchell@durham.ac.uk (JAJM), chris.done@durham.ac.uk (CD)

explicitly in Kubota & Done (2018, hereafter KD18), who used AGN of similar mass around $10^8 M_{\odot}$ but changing L_{bol} . (NGC5548, Mrk509, and PG1115 + 407) to demonstrate the systematic change in SED shape for $L/L_{\text{Edd}} \sim 0.03\text{--}0.5$. These AGNs are all above the transition value, but at the lower end of the luminosity range they show spectra that have strong hard X-ray emission, with similar power to that seen in the UV, while the spectra become systematically more UV disc dominated with increasing L/L_{Edd} .

The amount of disc to X-ray luminosity is often characterized by α_{ox} , the spectral index of a power law connecting from the UV (2500 Å) to the X-ray band at 2 keV. This index becomes progressively more negative with increasing L_{bol} , indicating that the spectra become more disc dominated (Lusso et al. 2010; Lusso & Risaliti 2016b). However, given the range of SMBH masses, it is not clear whether this trend (which does have scatter) is driven by L_{bol} or by $L_{\text{bol}}/L_{\text{Edd}}$ or a separate factor. Understanding the origin of this correlation would reduce the scatter, and give more accuracy as well as more confidence in its use as a cosmological probe (Lusso et al. 2018).

Another key difference between the BHB and SMBH at luminosities above the transition is the appearance of an additional component in the spectrum, between the disc and X-ray tail. There is a downturn in the UV which appears to connect to an upturn at soft X-ray energies above the 2–10 keV power law (soft X-ray excess). The origin and nature of this are not well understood, but it can be fairly well fit as a warm Comptonization component, in addition to a separate hot Comptonization component producing the X-ray tail (Gierliński & Done 2004; Porquet et al. 2004; Jin et al. 2012).

These differences show that there must be something that breaks the scaling between the SMBH and BHB above $0.02L_{\text{Edd}}$. One key theoretical difference is that the disc temperature in AGN is lower, $T_{\text{peak}} \propto (\dot{m}/M)^{1/4}$, where $\dot{m} = L/L_{\text{Edd}}$, at the innermost stable circular orbit, giving a predicted peak luminosity in the UV for AGN rather than in the soft X-rays as seen in BHB. This means that atomic physics should be very important in AGN discs, whereas the soft X-ray BHB discs are mostly dominated by plasma physics. This change in opacity could drive turbulence/convection, or even mass-loss via UV line driven disc winds (e.g. Laor & Davis 2014).

Another expected theoretical difference is that radiation pressure is much more important in SMBH discs. The typical density of the SMBH disc is lower as well as its temperature, so the gas pressure in the disc is lower for a given temperature. So radiation pressure within the disc can dominate over gas pressure inside the disc over a much wider radial range compared to the BHB at similar Eddington fraction, \dot{m} (Laor & Netzer 1989). This again could lead to turbulence/convection, and all hydrodynamic turbulence couples to the MRI dynamo which is the source of the viscosity, enhancing the heating towards the disc surface and potentially producing the warm Comptonization region (Jiang & Blaes 2020).

KD18 built a phenomenological model (QSOSED) to describe the changing SED in their very small sample of very well-studied AGN of fixed mass ($M_{\text{BH}} \sim 10^8 M_{\odot}$). This model is based on the expected Novikov–Thorne heating rate from a disc at a given M_{BH} and L/L_{Edd} , but incorporates a phenomenological prescription for how the energy is emitted, either as a standard disc (outer radii), warm Comptonization (mid-radii) or hot corona (inner flow). Kynoch et al. (2023, hereafter K23) have assembled a much larger sample of AGN with good-quality spectral data and thus fairly well-defined SEDs spanning the optical/UV and X-ray bandpass where most of the accretion energy should be emitted (detailed in Section 2.1). We use this new sample to critically test the QSOSED model across a wide range in mass and L/L_{Edd} with the aim of understanding and characterizing the accretion disc structures in AGN.

We first present an overview of the SOUX sample as defined in K23 along with a description of the models used throughout this work. We perform stacked fitting on the SOUX sample, binning on M_{BH} and L_{2500} . Using the insights gained from these fits we investigate the shape of the optical-UV continuum in the wider parameter space by constructing wider bandpass spectra from all of Sloan Digital Sky Survey (SDSS). These show no change in the optical-UV continuum at constant L_{2500} for changing mass by 2 dex. This is not compatible with any current accretion disc model. Even if the highest black hole masses are overestimated, the amount of fine-tuning required to match this looks contrived. Instead, we favour solutions where either the accretion disc is completely covered by a warm comptonizing layer whose properties change systematically with L/L_{Edd} , or the accretion flow structure is fundamentally different to that of the standard disc models.

2 THE SAMPLE AND DATA

K23 includes a detailed description of the sample selection, spectral fitting procedures, and calculation of important parameters such as black hole mass and radio loudness. We include a short summary here for completeness.

2.1 Sample selection

Our sample is primarily composed of sources taken from the Quasar Catalog of the Fourteenth SDSS Data Release (SDSS-DR14Q; Pâris et al. 2018) cross-matched with the fourth source catalogue of *XMM-Newton* (4XMM-DR9; Webb et al. 2020). In order to have good-quality X-ray spectra we only select sources with ≥ 250 counts in *XMM-Newton* without flags for high background, diffuse emission, or poor-source properties. The simultaneous OM optical/UV data are taken from the fourth *XMM-Newton* Serendipitous Ultraviolet Source Survey (XMM-SUSS4.1; Page et al. 2012).

We consider all AGN with $z \leq 2.5$ so as to have black-hole mass from Mg II. We perform a visual inspection of each optical spectrum and remove any BAL's, Seyfert 2 sources and any object with an unreliable black hole measurement due to poor or contaminated line profiles, i.e. line profiles displaying obvious absorption. Through this process, we obtain 633 sources. We then supplement this sample with a population of narrow-line Seyfert 1 (NLS1) sources taken from Rakshit et al. (2017, R17). By repeating the same selection process with this catalogue, we obtain 63 NLS1 not present in our previous sample, bringing the total number of sources to 696. Where $z \geq 0.4$ we discard any OM filter contaminated by the strong Ly α $\lambda 1216$ UV emission line.

2.2 Spectral fitting and black hole mass estimates

Rakshit, Stalin & Kotilainen (2020, hereafter R20) analyse the SDSS-DR14Q spectra using a modified version of the PYTHON PYQSOFIT package (Guo, Shen & Wang 2018; Guo et al. 2019; Shen et al. 2019). We fit the additional NLS1 sources from R17 with a version of PYQSOFIT modified to match the version used in R20. For the 84 sources in both R17 and R20, we compared our fits with those detailed in R20 and found good agreement.

All black hole masses were calculated from full width at half-maximum (FWHM) measurements described above, using the scaling relations detailed in Greene et al. (2010), Mejía-Restrepo et al. (2016), and Woo et al. (2018).

As our sources extend out to a redshift of 2.5, we are able to measure black-hole masses from either the H α , H β , or Mg II

broad emission lines. Where several of these are present we prioritize $H\beta$, then $Mg\text{II}$, followed by $H\alpha$. However, we also visually inspect each optical SDSS spectrum and choose a different line in cases where the ‘preferred’ option was clearly of lower quality.

2.3 Radio properties

Our 696 sources were cross-matched with both the Very Large Array (VLA) Faint Images of the Radio Sky at Twenty-Centimeters (FIRST) Becker (White & Helfand 1995) and the National Radio Astronomy Observatory (NRAO) VLA Sky Survey (NVSS; Condon et al. 1998) catalogues using a matching radius of 10 arcsec following Lu et al. (2007). Both surveys sample the sky at 1.4 GHz, FIRST has a beam width of 5.6 arcsec and NVSS of 45 arcsec. We matched 124 and 83 objects in FIRST and NVSS, respectively.

We converted $F_{1.4\text{GHz}}$ to $F_{5\text{GHz}}$ using the scaling relation $(\nu_{5\text{GHz}}/\nu_{1.4\text{GHz}})^{-\alpha_R}$, where α_R is a common spectral index of 0.6. These $F_{5\text{GHz}}$ values were converted to rest frame $L_{5\text{GHz}}$ using the method of Alexander et al. (2003). In objects where we have an $L_{4400\text{\AA}}$ and a FIRST detection, we calculated the radio loudness parameter, canonically defined as $L_{5\text{GHz}}/L_{4400\text{\AA}}$ (Kellermann et al. 1989).

Throughout the following analysis, 60 very radio loud sources (radio loudness > 100) were removed as there is a strong possibility that the jet emission dominates over that of the accretion flow itself. The most obvious example of this in the original sample is PMN 0948 + 0022, a NLS1 where the X-rays are clearly dominated by the jet emission that extends up to Fermi GeV energies (Foschini et al. 2012).

2.4 Sample pruning

K23 did not perform a detailed inspection of the broad-band SEDs or X-ray spectra in their analysis. Since in this work it is our goal to model the SEDs, we visually inspected each SED individually and removed any object with strong indicators of intrinsic (host) absorption. This could be due to cold/dusty gas in the molecular torus, easily seen as both the X-ray and UV data points are strongly attenuated at the lowest/highest energies, respectively. We also excluded objects with partially ionized, warm absorption from nuclear winds, identified as a sharply concave soft X-ray shape (Reynolds & Fabian 1995; Chakravorty et al. 2009).

This removed 54 sources from the original SOUX AGN sample of 696, described in K23, leaving 642 sources available for detailed analysis, this shall henceforth be referred to as the SOUX AGN sample. The 54 sources that have been removed from the sample before the fitting process are detailed in Table D1.

3 THE AGNSED/QSOSED MODELS

3.1 Review of SED models for the accretion flow

We use several different SED models in this work, so here we outline each one in turn. All of them are based on the emissivity of an optically thick, geometrically thin accretion disc in full general relativity (Novikov–Thorne, $\epsilon_{NT}(r)$) (Novikov & Thorne 1973). They give the luminosity emitted over a disc annulus as $L(r) = 2 \times 2\pi r \epsilon_{NT}(r) dr$.

3.2 Standard disc

The standard disc models assume that the disc luminosity as each annulus is emitted as a black-body spectrum in which the spectral radiance density $B_\nu(T_{\text{eff}})$ is a function of the effective temperature T_{eff} and the luminosity at a given radius $L(R) = \sigma_{\text{SB}} T_{\text{eff}}^4$. Pure standard disc models are where this holds over the entire disc, from R_{out} to R_{ISCO} . This is the model which is most often used to fit the optical/UV spectra, but it cannot produce the soft and hard X-ray emission observed from AGN.

3.3 Standard disc with colour temperature correction

The standard disc is the best physically understood model for the underlying accretion flow structure, but the best detailed calculations incorporate radiative transfer through the standard disc vertical structure. These calculations predict a shift of the observed disc emission to higher temperatures (Hubeny et al. 2001, D12). The standard disc energy is mostly dissipated close to the mid-plane, so it diffuses outwards, setting up a vertical temperature gradient through the optically thick material until it reaches the photosphere and escapes to the observer from an effective optical depth $\tau_{\text{eff}} = \sqrt{\tau_a(\tau_a + \tau_s)} \sim 1$ where τ_a and τ_s are the optical depth to true absorption and scattering, respectively. True absorption opacity depends on the density and temperature of the material, and decreases with frequency, while electron scattering is a constant. Thus, a single radius in the disc has a spectrum which follows the expected black-body emission only for $h\nu \ll kT_{\text{eff}}$, where $\tau_a \gg \tau_s$, but the higher frequencies are dominated more by scattering, moving the photosphere deeper into the disc vertical structure, where it samples higher temperature emission. This effect becomes apparent for photosphere temperatures $T_{\text{eff}} \geq 3 \times 10^4$ K, and is fairly well approximated by a changing colour temperature correction, f_{col} so that each radius emits a spectrum which can be approximated as $B_\nu(f_{\text{col}} T_{\text{eff}})/f_{\text{col}}^4$ where $f_{\text{col}} = 1$ for $T_{\text{eff}} < 3 \times 10^4$ K. This produces a slight flattening of the spectrum in the UV, as the radii which would have emitted at this energy are shifted to higher apparent temperature, making the disc spectrum peak at higher energies. However, it still cannot produce the soft or hard X-ray tail. This model is utilized in Section 5.3.

3.4 AGNSED, including soft, and hard Comptonization

The model AGNSED, described in KD18, is more flexible as it allows the accretion energy to be emitted as soft and hard Comptonization as well as disc blackbody. These are tied together by the underlying assumptions that the energy is from accretion and that the flow is in a radially stratified such that the emission only thermalizes to a blackbody for $R > R_{\text{warm}}$. For $R_{\text{warm}} < R < R_{\text{hot}}$, the power is instead emitted as an optically thick, warm Comptonization component, largely in the soft-X-rays (described by its photon index Γ_{warm} and electron temperature $kT_{e,\text{warm}}$, with seed photon temperature set by the underlying disc), while below R_{hot} the spectrum switches to hot, optically thin Comptonization (parameters Γ_{hot} and $kT_{e,\text{hot}}$) from the corona, largely emitting in the hard X-rays.

This has enough flexibility to fit the entire SED of the accretion flow from optical-UV and X-ray, but has a number of free parameters describing the non-standard disc sections of the flow.

3.5 The QSOSED phenomenological model

KD18 fit AGNSED to the SED of three AGN of similar mass, but spanning a range of L/L_{Edd} . Their analysis showed that the power

dissipated in the hot Comptonization region was approximately constant at $0.02L_{\text{Edd}}$. This is the maximum ADAF luminosity, defining the hard–soft transition luminosity, but its persistence above the transition is not what is expected from BHB. The BHB can show very disc dominated spectra above the spectral transition i.e. with hot Comptonization power $\ll 0.02L_{\text{Edd}}$.

Another difference between the AGN and BHB SEDs is that AGN at $L < 0.1L_{\text{Edd}}$ show hard X-ray spectra, with $\Gamma_{\text{hot}} < 1.9$, whereas the BHB always show soft spectra, with $\Gamma_{\text{hot}} > 2.0$ above the transition. This difference is important as it is difficult to produce hard spectra. An isotropic X-ray corona above a disc must have $\Gamma_{\text{hot}} > 1.95$ due to reprocessing. Not all the photon energy illuminating the disc from the corona can be reflected, especially for hard spectra where the luminosity peaks at ~ 100 keV. Compton downscattering on reflection means that at least 30 percent of the illuminating flux goes instead into heating the disc, producing a reprocessed thermal component which is re-intercepted by the corona. Even if the disc is completely dark (passive), so that all the accretion energy is dissipated in the corona, these reprocessed photons give a lower limit to the seed photons such that $L_{\text{seed}} \sim L_{\text{x}}$, which ties the X-ray spectral index to $\Gamma_{\text{hot}} \sim 2$ (Haardt & Maraschi 1991, 1993; Stern et al. 1995; Malzac et al. 2003). Thus, the AGN with spectra $\Gamma_{\text{hot}} < 1.9$ most likely still have a truncated disc geometry, unlike the BHB above the transition (KD18).

The QSOSED model folds all these results into a predictive model for AGN SED. Firstly, it calculates the truncation radius assuming that the hot X-ray plasma replaces the inner disc from R_{isco} out as far as required for the accretion disc power to reach $0.02L_{\text{Edd}}$. Thus, $R_{\text{hot}} \gg R_{\text{isco}}$ for an AGN at $L_{\text{bol}} = 0.03L_{\text{Edd}}$, leaving very little power for the outer UV disc emission. Conversely, for an AGN at $L_{\text{bol}} \sim LL_{\text{Edd}}$, $R_{\text{hot}} \sim R_{\text{isco}}$ so its SED is dominated by a UV bright disc component. This geometry and energy balance is used to calculate the self-consistent power-law index of the hot Comptonization region, Γ_{hot} , fixing its spectrum in both normalization and index assuming that the electron temperature remains fixed at 100 keV (KD18).

The warm Comptonization region is even less well understood than the hot Comptonization, but it can be fit with optically thick material (with optical depth $\tau \sim 10$ – 20) which makes it look like it is associated with the disc, perhaps due to the dissipation region moving upwards toward the photosphere, as opposed to the standard Shakura–Sunyaev disc where the dissipation is mainly in the equatorial plane. In this case, Compton reprocessing again sets the energy balance between the seed photons and electron heating. The difference is that for the observed low temperature of ~ 0.2 keV, this gives $\Gamma_{\text{warm}} \sim 2.5$ (Petrucci et al. 2018; KD18). The QSOSED model fixes these parameters, but needs also the transition radius, R_{warm} at which the disc stops emitting as a black-body standard disc, and instead produces the warm Comptonization region. Since this is not understood theoretically, KD18 took it from the data which could be described by $R_{\text{warm}} = 2R_{\text{hot}}$.

Thus, the QSOSED model contains a number of assumptions in addition to those of AGNSED (emissivity given by Novikov–Thorne thin disc, but the emission mechanism is radially stratified):

- (i) The hard X-ray luminosity is $0.02L_{\text{Edd}}$ irrespective of L_{bol} .
- (ii) The temperature of the warm Comptonized disc is ~ 0.2 keV, and it is a passive structure so $\Gamma_{\text{warm}} = 2.5$.
- (iii) The warm Compton region extends from $R_{\text{warm}} = 2R_{\text{hot}}$.

The SOUX sample can test many of these assumptions as we have many more than the three SEDs used by KD18, and it spans a larger range in \dot{m} and a much larger range in M_{BH} .

3.5.1 Example QSOSED spectra

Fig. 2 shows the model SED for changing L/L_{Edd} (in steps of $\log(L/L_{\text{Edd}}) = 0.1$) for black hole mass of $5 \times 10^7 M_{\odot}$ (left) and $5 \times 10^9 M_{\odot}$ (right) for $\log(\dot{m}) = -1.645 - 0.355$ (corresponding to $0.026 < L/L_{\text{Edd}} < 2.6$). The model is only defined over this range as below the lower limit, AGN should make a changing look transition to be completely dominated by the X-ray hot flow (ADAF), and above the upper limit, the effects of optically thick advection/winds should become apparent, changing the emissivity to that of a slim disc (Abramowicz et al. 1988; Kubota & Done 2019).

These figures show the effect of the assumptions of the QSOSED model. For both masses, the R_{hot} and Γ_{hot} values are the same at a given \dot{m} , with R_{hot} decreasing from $(155-9)R_{\text{g}}$ as \dot{m} increases from 0.026 to 2.6 (see Fig. 3), so that the disc and warm Comptonization regions progressively dominate more of the emission. However, M_{BH} has an impact on the SED as the outer disc temperature and seed photon temperature for the warm disc region are lower at the higher black hole masses. The 2500 Å flux (indicated by the vertical dashed lines in Fig. 2) is generally mostly produced in the outer standard disc region for the lower mass AGN ($5 \times 10^7 M_{\odot}$). However, for the higher mass of $5 \times 10^9 M_{\odot}$, the outer disc generally peaks below 2500 Å, so the UV flux is instead dominated by the warm Comptonization up to $\sim 0.1L/L_{\text{Edd}}$. Thus, the model predicts a mass dependence to the α_{ox} values due to the difference in UV emission mechanism with mass, as well as a dependence on \dot{m} .

These model SEDs also show how to understand the lines of constant L/L_{Edd} overlaid on Fig. 1. A pure disc spectrum should have $L_{2500} \propto (M_{\text{BH}}^2 \dot{m})^{2/3}$. Both high and low masses are dominated by the disc at the highest \dot{m} , so the grey lines of constant $\dot{m} \gtrsim 0.5$ have $L_{2500} \propto M_{\text{BH}}^{2/3}$, a non-linear relation, unlike the constant bolometric correction which is often assumed, where $L_{2500} \propto M_{\text{BH}}$. At lower \dot{m} , the highest masses start to bend away from this expected slope as the lower standard disc temperature means the UV is dominated by the warm Comptonization region rather than the standard disc. Here and throughout, L_{2500} refers to the monochromatic luminosity at 2500 Å (in units of erg s^{-1}).

There is an especially sharp decrease at the lowest \dot{m} for the highest masses. This is because of the assumption that the outer radius of the disc is set by self-gravity. The self-gravity radius (R_{sg}) is only a few hundred R_{g} for the most massive AGN at the lowest \dot{m} (see Fig. 3). The QSOSED model has the accretion flow end before making the transition to a thin disc for masses above $2 \times 10^8 M_{\odot}$. Above this mass the warm Compton region gets smaller and smaller, extending across $(155-311)R_{\text{g}}$ at $2 \times 10^8 M_{\odot}$, but shrinking to $(155-167)R_{\text{g}}$ at $5 \times 10^9 M_{\odot}$ for $\dot{m} = 0.026$ (see Fig. 3). This dramatically reduces the warm Compton emission, leading to an extremely hard X-ray spectrum.

However, the extent of the disc is very uncertain as the self-gravity radius is calculated here assuming that the disc surface density is set by the standard Shakura–Sunyaev disc in the radiation-pressure-dominated regime (Laor & Netzer 1989), yet the SED at low \dot{m} is very unlike a standard disc. There is no clear picture from observational data either, with some studies finding the disc to be larger (e.g. Hao et al. 2010; Landt et al. 2023), others smaller (e.g. Collinson et al. 2017). The green-dashed line in Fig. 2(b) shows the effect of increasing the disc outer radius to a generic value of $10^5 R_{\text{g}}$ in the QSOSED model. This gives a dramatic increase in the UV and especially the optical luminosity, with the outer standard disc region now evident in the SED at the lowest frequencies. This shows that the optical/UV spectra of the highest mass AGNs are sensitive to the outer extent of the disc.

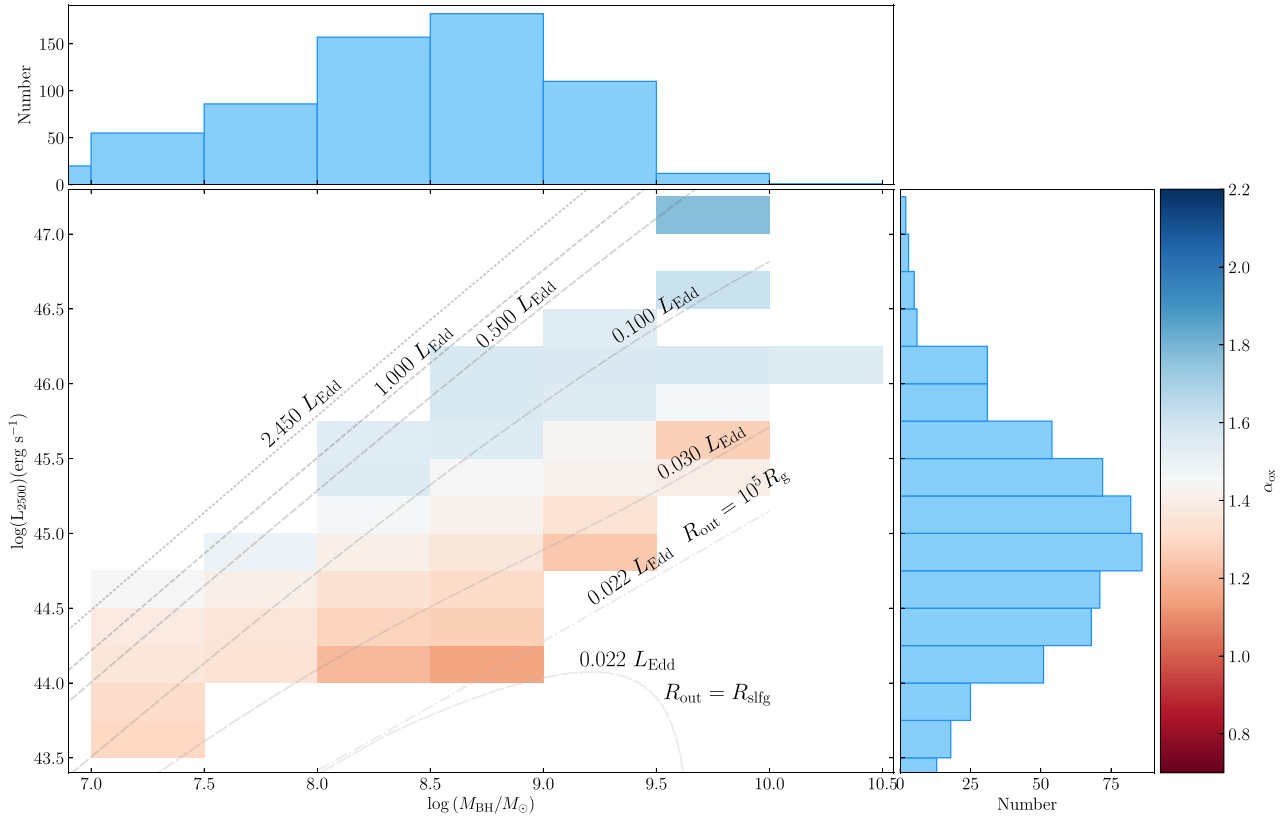


Figure 1. Black hole mass against $\log(L_{2500})$ both measured from SDSS optical spectra. Each grid point bin of 0.5 dex in mass and 0.25 dex in $\log(L_{2500})$ contains at least 5 objects, or 1 object for $\log(M_{\text{BH}}/M_{\odot}) \geq 9.5$ enabling us to expand the sample to higher M_{BH} . **K23** show a similar plot for the full sample, but here we show only the curated sample, i.e. removing 60 very radio loud sources (radio loudness > 100) to avoid potential contamination from the jet, and removing an additional 54 sources which display clear signs of intrinsic cold or warm absorption. Lines of constant \dot{m} calculated from QSOSED are overlotted.

Fig. 2(b) also shows that the QSOSED spectra for the highest mass AGNs are predicted to peak in the observable optical/UV for $\dot{m} < 0.1$. Thus, it is the highest mass AGN at the lowest \dot{m} which are most sensitive to the standard disc region and how (or if) this transitions to the warm Comptonized region. Instead, the lowest mass AGN at the highest \dot{m} are most sensitive to the transition from warm Comptonization to hot Comptonization. These low mass, highest \dot{m} are also the ones which are most likely to be at low redshift, maximizing the visibility of the soft X-ray excess in the XMM bandpass.

Thus the predictions of the QSOSED model can be directly tested on our new sample of AGN which span a wide range of mass and \dot{m} .

4 FITTING TO THE DATA

Throughout this section we consider the mean SED from the data in each grid point, comparing it to a series of models. For the first two Sections 4.1 and 4.2, we only fit to the UV data from the OM, and then extrapolate to the optical SDSS and X-ray bandpasses, forming a true test of the model predictions. We only include the X-ray data in the fit in Section 4.3. We never include the SDSS data in the fits as this is not simultaneous, so variability could distort the modelling. However, this is minimized by averaging over all the objects in the bin, and the generally good match between the SDSS and OM data provides a check on intercalibration/aperture issues.

We make the mean SED from the data by fitting a single model for each grid point, with black hole mass fixed at the (logarithmic) centre of the mass gridpoint. This model is fit simultaneously to the relevant spectral range of all objects in that bin, but with parameters set to the individual objects co-moving distance/redshift, and appropriate galactic reddening/absorption. The data of each object is plotted in $\log \nu$ versus $\log \nu L_{\nu}$, where the data are shifted into the rest frame of the galaxy and corrected for galactic absorption by considering the dust maps of Schlafly & Finkbeiner (2011) using the ASTROPY extinction module with the (Cardelli, Clayton & Mathis 1989) extinction profile. Each instrument for each individual source is rebinned on to a common energy grid (six bins for *XMM-Newton* and four for the OM). We calculate a weighted log mean of all the data for each bin, with any data point with an intersecting energy uncertainty being included. The weighted 1σ standard deviation for each bin is displayed either side of the weighted mean.

Similarly the composite SDSS optical spectra for each bin are the geometric mean of the de-reddened, redshift corrected individual spectra, again with weighted $\pm 1\sigma$ standard deviation. We bin in log space as this means that the spectral slope of the composite has the mean of the spectral slopes of the individual spectra from which it is composed (see Reichard et al. 2003).

All plots containing SED insets follow the same format as described above, and each inset plot spans 2 dex in luminosity and covers the spectral range between $10^{14.2}$ and $10^{19.6}$ Hz.

4.1 QSOSED in each $M_{\text{BH}}-L_{2500}$ bin

QSOSED can be used to create an entire SED from a single data point so we test this by fitting *only* to the mean UV data and extrapolating the resultant model down through the optical and up into the X-ray bandpass. We fix black hole spin at $a_* = 0$, so \dot{m} is the only free parameter, essentially fixing it to give the mean L_{2500} of each grid point. We show the results of this fit, hereafter called QSOSED UV-tied, in Fig. 4.

Each inset plot shows the QSOSED fit (solid line) together with the SDSS optical (red), *XMM-Newton* OM UV (blue) and X-ray (pink) data for all objects located in each respective gridpoint. We stress that the QSOSED UV-tied model is fit only to the UV data, not to the X-ray or optical points on this plot, yet to zeroth order the QSOSED model is in broad agreement with both the optical and X-ray data. The range of resultant \dot{m} match the grey lines plotted in Fig. 1, as expected given that these fits are forced to match the L_{2500} luminosity. These are spin zero models, but in general the entire SED is well fit. Extreme spin gives a factor of 6 more luminosity for the same mass accretion rate through the outer disc. There is no strong evidence for this. Strong wind losses would reduce the mass accretion rate through the innermost regions of the disc. We might expect this to be most important at the highest \dot{m} but there is no clear trend of the X-ray flux being strongly overpredicted. To within factors of a few, the thin disc emissivity which is hardwired into QSOSED is giving the correct bolometric flux for a zero spin black hole.

To first order though, there are some interesting discrepancies. At low masses, $\log(M_{\text{BH}}/M_{\odot}) < 8.0$, the optical data are systematically higher than the model especially at low \dot{m} , so that the optical/UV spectra are redder than the standard outer disc spectrum assumed in the model. This could be due to host galaxy contamination, which should become more prominent for low black hole mass, low-luminosity AGN (Done et al. 2012, hereafter D12). The X-ray data are also systematically ~ 0.5 dex higher than the model for these lower black hole masses at high \dot{m} , so require more than the assumed 2 per cent of power dissipated in the hot coronal region (see also Middei et al. in preparation).

However, the major discrepancies are all at the highest masses, $\log(M_{\text{BH}}/M_{\odot}) > 9.0$. The QSOSED model systematically overpredicts the X-ray by $\sim (0.3-0.6)$ dex in luminosity for all values of \dot{m} . Most surprisingly though, the optical/UV slope in the data is generally much bluer than the model. This is not likely to be from any aperture difference between SDSS and OM as the galaxy contamination should be negligible at these high luminosities. The optical/UV data simply do not look like a standard outer disc for a black hole of this mass and mass accretion rate. The observed optical/UV spectra in this mass range are still typically rising towards Ly α but the QSOSED models predict that the emission should peak below this energy. As seen in the model spectra shown in Fig. 2, stronger outer disc emission could easily be produced by increasing the outer disc radius. However, this further decreases the characteristic energy at which the disc components peak, whereas the data show that the QSOSED model (with its very small outer radius from self-gravity) already predicts the peak energy being too low. In essence, the optical/UV data do not look like the QSOSED models in this range, as the outer standard disc in the model peaks at too low energy.

This is very surprising, especially as the outer standard disc is the least controversial of all the QSOSED components. The UV spectrum could be suppressed by dust reddening from the host, but this would make the mismatch worse as these high-mass AGN have spectra that are already too blue to match the standard disc.

The spectrum rather appears like a standard disc, but shifted over to higher energies than predicted for black holes of this high mass for a wide range in mass accretion rate. Section 5 considers the optical/UV spectral shape in more detail, and shows that this mismatch at the highest masses is not due to the assumption in QSOSED that the warm and hot Comptonization power is derived from the disc. Even pure disc models, where all the power is dissipated in blackbody emission down to R_{isco} of a high spin black hole cannot match the far UV emission in the spectra observed in the high mass/low \dot{m} bins.

Interestingly, where the QSOSED models fit the SEDs (highest \dot{m} for $\log(M_{\text{BH}}/M_{\odot}) > 8$), their predicted EUV continuum is able to match the observed 1640 Å He II equivalent widths (Temple et al. 2023).

4.2 Fully Comptonized outer disc: AGNSEED ($R_{\text{hot}} = 10R_g$) in each $M_{\text{BH}}-L_{2500}$ bin

One way to shift the disc spectrum to higher energies is if the whole disc is covered by the warm Comptonized layer. This was suggested by Petrucci et al. (2018) as they had noticed that the spectra of even the $10^8 M_{\odot}$ AGN seemed to be well fit with just warm and hot Comptonization, without the need for a standard disc once the host galaxy was subtracted.

We simultaneously fit all the OM data in a given grid point as before, only now we use the more flexible AGNSEED and fix $R_{\text{warm}} = R_{\text{out}}$ so that the entire outer disc is covered by the warm Compton layer. We again fix $\Gamma_{\text{warm}} = 2.5$ and $kT_{\text{warm}} = 0.2$ keV in this region. However, AGNSEED also allows freedom in R_{hot} and in Γ_{hot} , so we first fix these to $10R_g$ and 2.0, respectively in order to find the mean \dot{m} for each grid point. Setting R_{hot} at $10R_g$ is equivalent to fixing the power dissipated in hot corona to ~ 7 per cent of L_{bol} [see Fig. 3 for $\log(\dot{m}) = -0.5$].

The results from this fitting procedure (henceforth referred to as AGNSEED UV-tied $R_{\text{hot}} = 10R_g$) are displayed in Fig. 5. The background, as in Fig. 4, is colour coded to the \dot{m} value derived for the bin. These are shifted in a complex way from the values derived before. Fig. 6(a) shows the ratio of mass accretion rates derived from QSOSED and the AGNSEED UV-tied models. At lower mass/higher L_{2500} , the AGNSEED models need a higher \dot{m} than QSOSED, whereas the opposite is true at higher masses.

Fig. 6(b) shows why this is the case for each of these conditions (bins labelled 1 and 2). At the lowest masses (bin 1), the 2500 Å point (dashed line) is in the standard disc region of the QSOSED model (red), as can be seen by comparison to a completely standard disc model for the same \dot{m} (purple: $R_{\text{hot}} = R_{\text{warm}} = 6R_g$). Instead, a model with the same \dot{m} where the entire disc is covered by the warm Compton region (black: $R_{\text{hot}} = 6R_g$, $R_{\text{warm}} = R_{\text{out}}$) has much lower luminosity at 2500 Å. This is because the warm Comptonization shifts the disc spectrum to higher energies, acting like a colour temperature correction. Hence, to match the data at 2500 Å requires a higher \dot{m} (dashed black line).

Instead, for the highest masses, the behaviour is opposite as the QSOSED model (red) already had the 2500 Å flux produced by the warm Comptonization rather than the outer standard disc. A completely standard disc (purple: $R_{\text{hot}} = 6R_g$, $R_{\text{warm}} = 6R_g$) is again shown for comparison. Completely covering the disc with the warm Comptonization with the same \dot{m} (black: $R_{\text{hot}} = 6R_g$, $R_{\text{warm}} = R_{\text{out}}$) now overpredicts the 2500 Å flux, so here the data require a lower \dot{m} to match the data than before (dotted black line).

This complex change in \dot{m} across the large range in M_{BH} and L_{2500} increases the range of \dot{m} spanned by the sample. The lowest \dot{m} values

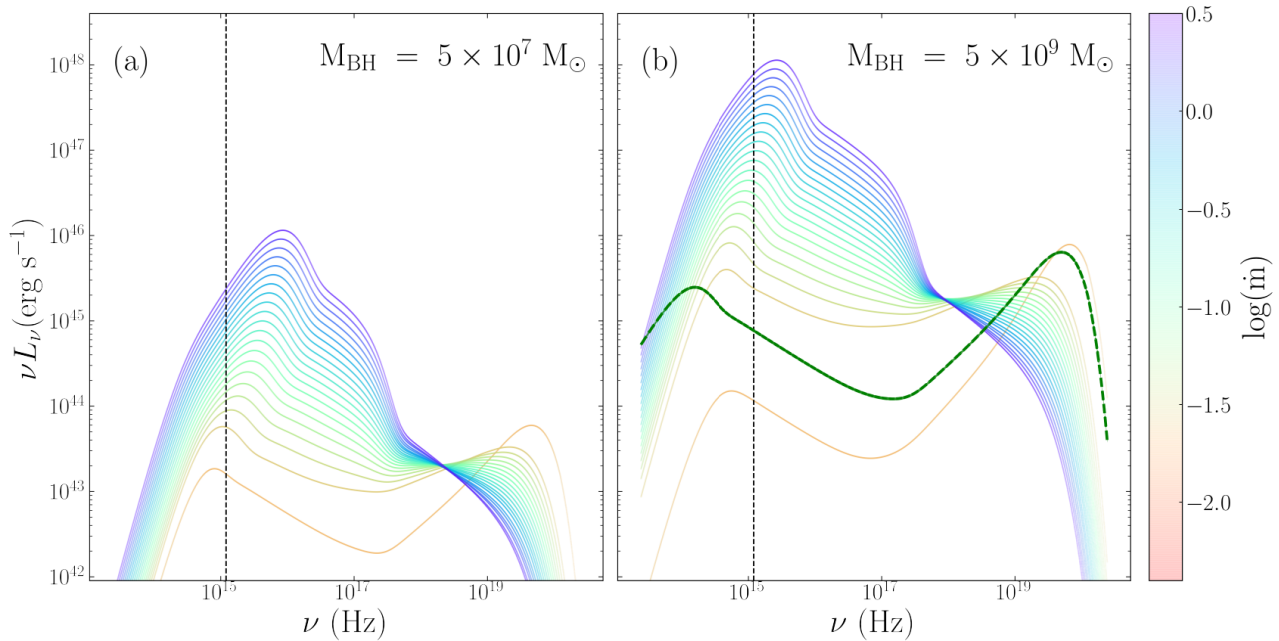


Figure 2. QSOSED predictions for the SED for black holes of mass $5 \times 10^7 M_{\odot}$ (a) and $5 \times 10^9 M_{\odot}$ (b) for a range of mass accretion rates assuming spin 0. The 2500 Å point is indicated by the vertical dashed line on each panel. The green line in the right-hand hand (high black hole mass) panel shows the effect of increasing the outer disc radius from the (small) self-gravity radius to a value of $R_{\text{out}} = 10^5 R_g$ at the lowest L/L_{Edd} .

are now well below $\dot{m}=0.02$, so this loses the correspondence of the ‘changing look’ transition in AGN with the soft-hard transition from a disc to ADAF-like state in BHB (e.g. Noda & Done 2018; Ruan et al. 2019).

Nonetheless, Fig. 5 shows that the new model has the desired effect in giving a much better match to the optical/UV spectra at high black hole masses, but now the optical/UV from the lower mass black holes are not well fit.

Unlike the mismatch with the standard disc in the highest mass AGN where the data were already too blue, here the data are too red. Hence the models could be made to fit the data if there was either internal reddening suppressing the UV, or host galaxy contamination enhancing the optical, or a combination of both. K23 assess the broad line region Balmer decrement across the sample, but show that this has no clear relation with the optical/UV continuum slope (their Section 4.1). Additionally, we have pruned the full sample, removing all objects with obvious internal reddening (Section 2.4). K23 also assess the host galaxy contamination (their Section 3.1) but conclude that this is negligible below 4400 Å. Thus these effects are unlikely to provide a full explanation of the observed discrepancies, especially as there are additional tensions in the SEDs. The model now overpredicts the soft X-ray excess, most clearly in the higher luminosity bins with $\log(M_{\text{BH}}/M_{\odot}) < 8.5$. A large soft X-ray excess is an inevitable result of assuming that all the disc power above $R_{\text{hot}} = 10R_g$ is Comptonised.

However, it is also clear that a fixed $R_{\text{hot}} = 10R_g$ is not compatible with the X-ray data. This is most clear in the $\log(M_{\text{BH}}/M_{\odot}) = 8.0$ – 8.5 bin, where this model systematically underpredicts the X-ray power at low \dot{m} , and overpredicts it at high \dot{m} . There is a very clear decrease in the ratio of hard X-ray to bolometric luminosity as a function of \dot{m} (see e.g. Vasudevan & Fabian 2007; Vasudevan 2008). Hence, we let the parameters of the hot Comptonization region be free to see if this can resolve the tensions seen here.

4.3 Comptonized outer disc: AGNSED fits to the mean SED using all XMM–Newton data

We still assume the outer disc is completely covered by the warm Comptonization region with $\Gamma_{\text{warm}} = 2.5$ and $kT_{\text{e,warm}} = 0.2$ keV but now allow freedom in the hot corona parameters of R_{hot} and Γ_{hot} in addition to \dot{m} . This requires that we fit the X-ray spectra as well as the UV data in each grid point. Fig. 7 shows the results of this. There is now a clear discrepancy in the normalization of the optical/UV model at lower masses. This is especially evident for $\log(M_{\text{BH}}/M_{\odot}) < 8.0$ at high \dot{m} , where now the UV normalization does not match the data. This is because the X-rays are now included in the fit as well as the UV, so the model is averaging between them. The model SED now has a strong soft X-ray excess as the entire outer disc is covered by a warm Comptonizing layer. The X-ray spectra do not generally support such a strong soft X-ray excess, so the fit compensates by reducing \dot{m} (which itself will reduce the size of the soft excess) and increasing R_{hot} . But this in turn overpredicts the observed X-ray luminosity in the 2–10 keV bandpass, so the fit pushes the X-ray spectral index to its hard limit of $\Gamma_{\text{hot}} = 1.6$ so as to put some of this power above 10 keV where there are no data.

Compared to QSOSED, this model gives a much better fit to the high M_{BH} , but a worse fit to the lower M_{BH} . Fig. 8 shows the resultant \dot{m} , R_{hot} , Γ_{hot} , and $L_{\text{disc, hot}}/L_{\text{Edd}}$ values for this model, compared to the same parameters for the original QSOSED UV-tied model. The region where Γ_{hot} pegs to the minimum value clearly shows the parameter space where the fits are least convincing.

5 THE SHAPE OF THE OPTICAL/UV SPECTRUM FROM SDSS

5.1 SDSS composites

We can make an independent check of the shape of the optical/UV spectrum using composites from a much larger sample of AGN

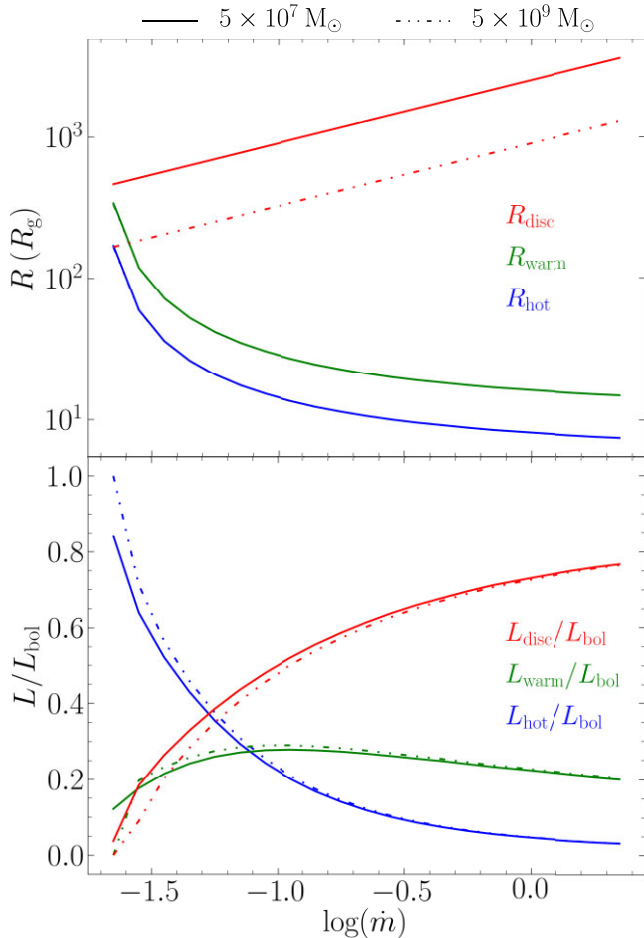


Figure 3. Radii and luminosities of each emission region of the QSOSED models shown in Fig. 2. Solid lines show results for $5 \times 10^7 M_{\odot}$, dashed show $5 \times 10^9 M_{\odot}$. *Top Panel:* The hot corona extends from R_{isco} to R_{hot} (blue), the warm corona extends from R_{hot} to R_{warm} (green), and the standard disc extends from R_{warm} to R_{out} (red). *Bottom Panel:* Corresponding luminosities in each component: $L_{\text{disc}}/L_{\text{bol}}$ (red), $L_{\text{warm}}/L_{\text{bol}}$ (green), and $L_{\text{hot}}/L_{\text{bol}}$ (blue).

in the SDSS DR14 quasar catalogue (Pâris et al. 2018). This contains 526 356 sources each possessing a publicly available optical spectrum.

5.1.1 Source selection and composite creation

We derive spectral composites which span a similar range in wavelength to our SDSS-OM bandpass by selecting objects with the same mass and 2500 \AA luminosity at both low and high redshift. We use a redshift cut at $z \leq 0.8$ and $2.15 \leq z \leq 2.25$ for H β and Mg II respectively. We remove any source with a poor-quality flag in z , L_{3000} or M_{BH} in addition to removing any source flagged as a BAL. In order to remove noisy spectra from the composites we carry out a signal-to-noise cut, removing any source with a continuum signal-to-noise ratio < 5 . This selects only ~ 4 per cent of the entire SDSS DR14 quasar catalogue

Each spectrum was de-reddened for the Galactic dust using the ASTROPY extinction module (Astropy Collaboration et al. 2018) assuming a CCM89 extinction profile (Cardelli et al. 1989) and an $R_V = 3.1$. The $E(B - V)$ measurements for each source were derived from the Schlafly & Finkbeiner (2011) dust maps and sourced from

the IRSA data base. The de-reddened spectra were resampled on to a uniform wavelength grid with a resolution of 5 \AA , converted to νL_{ν} and shifted into the rest frame.

Here and throughout, as with L_{2500} at 2500 \AA , L_{3000} refers to the monochromatic luminosity at 3000 \AA in units of erg s^{-1} . The spectra were binned on L_{3000} and M_{BH} according to the values quoted in R20. The (median $\pm 0.5\sigma$) discrepancy between L_{2500} and L_{3000} measured in the SOUX AGN sample was (0.05 ± 0.05) dex, so this small shift in wavelength will not affect the findings.

We calculated composite mean spectra for the high and low redshift samples separately, using the weighted geometric mean and weighted standard error at each wavelength element on the uniform wavelength grid. These composites for each of the bins populated by the SOUX AGN sample are shown in Fig. 9. The whole grid is shown in the Appendix (Figs B1 and B2). Many of the lower mass bins only contain low redshift spectra due to the lack of high-redshift sources in this mass range, the opposite effect is true for some of the higher mass bins in which there does not exist any low redshift sources.

Unlike the SOUX sample, Figs 4–8, we have not attempted to remove very radio loud sources as not all the SDSS spectra have $L_{4400 \text{ \AA}}$, so this cannot be done systematically, but this will only be a very small fraction of the sources, so their effect on the composites should also be small.

5.1.2 Comparison with QSOSED and AGNSED

Fig. 9 shows the same grid as seen in Fig. 1; however, each inset plot shows the average QSOSED (UV-tied, black), the average AGNSED model (UV-tied, red), and the SDSS composite spectra (low z : indigo, high z : purple) relevant to each bin.

The models plotted in Fig. 9 have not been exposed to the SDSS data meaning that the SDSS composite spectra provide a powerful diagnostic tool to assess the accuracy of our fits in both flux level and shape, and their relevance to the wider AGN population.

It is clear that, in general, the composite SDSS data from a wider sample of AGN are similar to the SDSS-OM spectra from the SOUX sample. At lower redshifts, we see spectral shapes much redder than the models which is consistent with our own SDSS spectra and UV data points, an effect that we attribute to host galaxy contribution to the spectra. In general, the composites show a better agreement with the QSOSED (black) models over the AGNSED (red) models at low to medium mass, but then shift towards the shape of our AGNSED (red) models at higher masses.

The trends seen in the optical/UV SDSS spectra shown here are similar to those seen in our SOUX sample. This shows that there is no significant selection bias in our sample introduced by the requirement for ≥ 250 counts in *XMM-Newton*, and the removal of extremely loud radio sources (Radio Loudness > 100).

5.2 Changing mass at fixed UV luminosity

The spectral shape of the optical-UV continuum from a pure disc remains constant on the Rayleigh–Jeans part of the disc, with monochromatic luminosity $\nu L_{\nu} \propto (M^2 \dot{m})^{2/3}$. However, we do not expect to be on the Rayleigh–Jeans tail in the rest frame UV for the wide range of masses sampled here. The green box in Fig. 9 shows we sample a mass range of at least 1.5 dex at a constant monochromatic luminosity, so the standard disc would have to change in \dot{m} by 3 dex. Even if the lowest mass bin was at $\log(\dot{m}) = 1$, the highest would have to be at $\log(\dot{m}) = -2$, around the changing look transition. The pure disc models at such low-mass

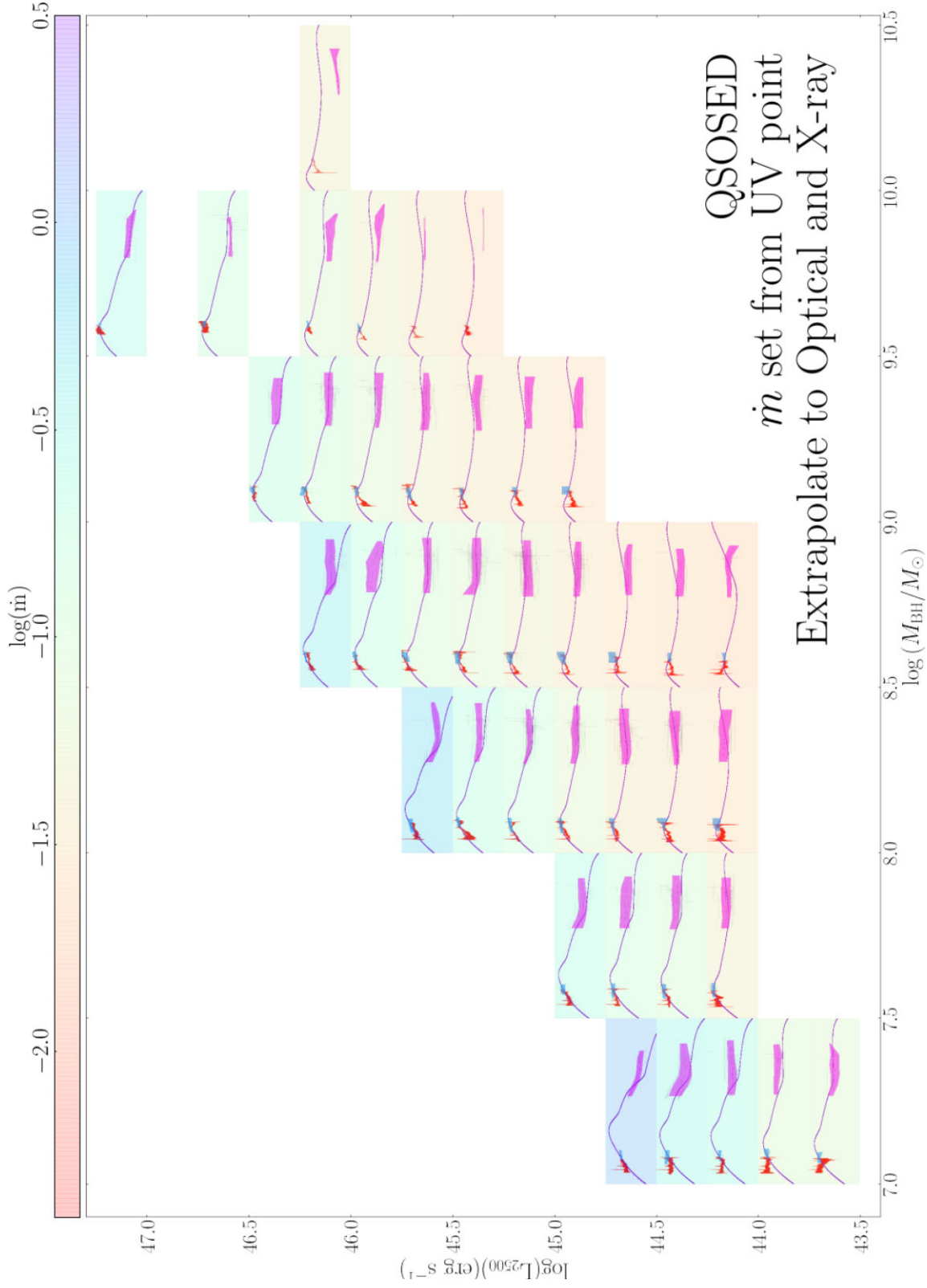


Figure 4. The same black hole mass–luminosity plane shown in Fig. 1, but now with inset in each bin showing the mean data SED from SDSS (red), OM (blue), and X-ray (pink) in that bin, together with the QSOSED UV-tied SED model. The only free parameter in these models is \dot{m} , and it is only fit to the UV data and then extrapolated across the whole spectrum. The background colour of each bin indicates the resultant $\log(\dot{m})$.

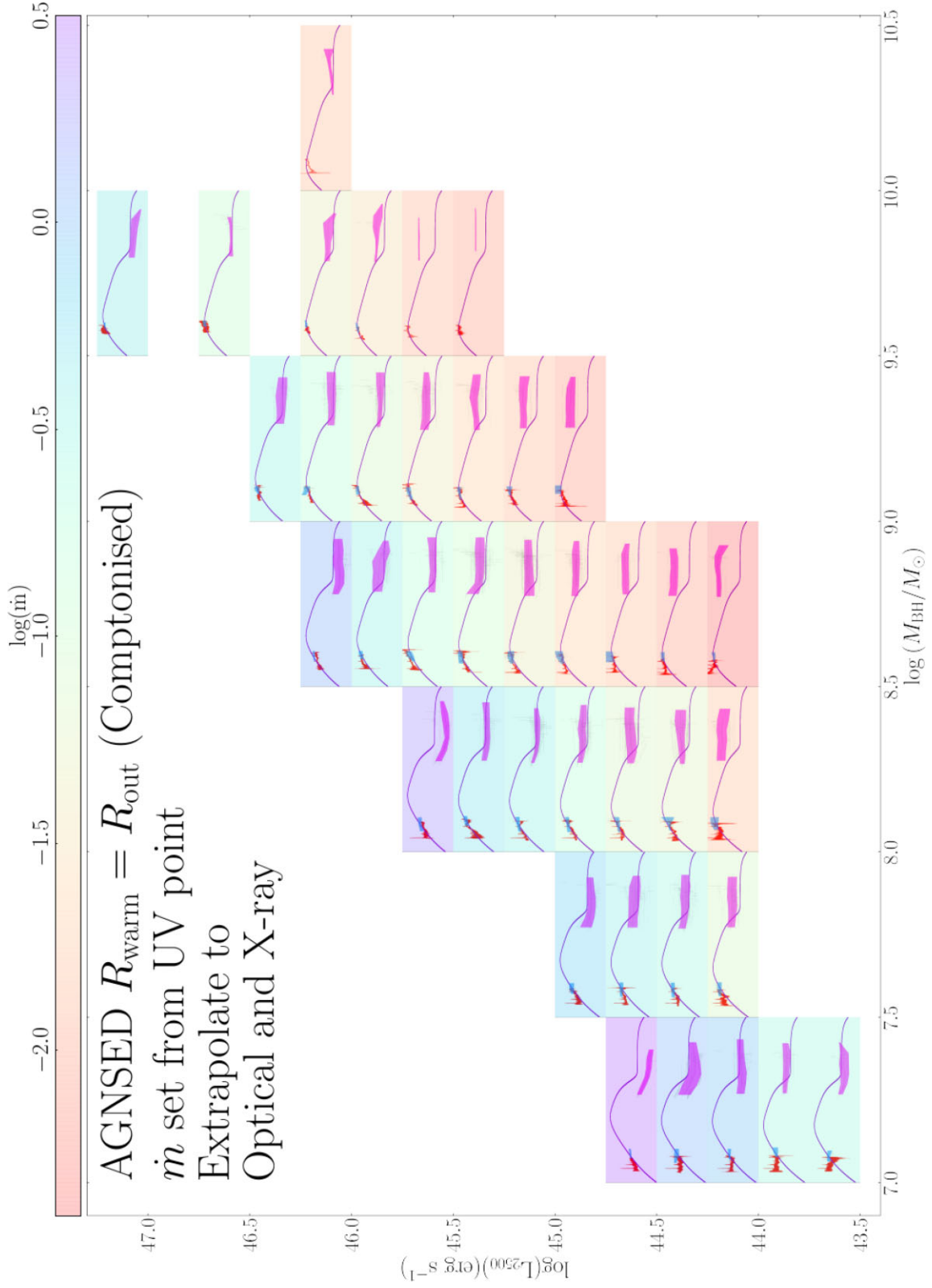


Figure 5. As in Fig. 4, but with the AGNSED UV-tied model. This has $R_{\text{warm}} = R_{\text{out}}$ so the entire outer disc is Comptonised, fixed $R_{\text{hot}} = 10R_{\text{g}}$ and $\Gamma_{\text{hot}} = 2.0$, so \dot{m} is the only free parameter. Again, this is fit only to the UV data points, and then extrapolated. The background colour in each bin indicates the resultant $\log(\dot{m})$, which is often quite different to that derived from the QSOSED UV tied models.

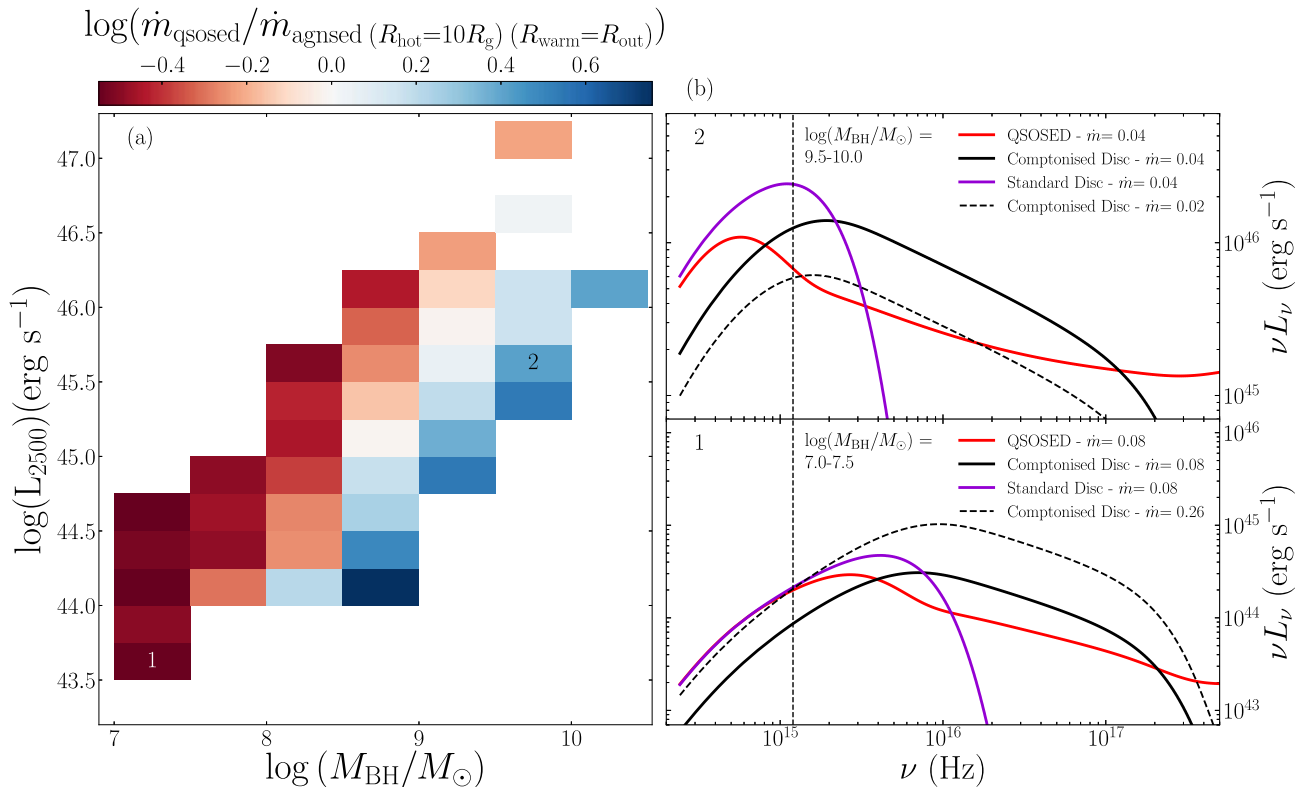


Figure 6. *Left-hand panel:* A comparison of the \dot{m} derived from the QSOSED UV-tied and AGNSED UV-tied models of Figs 4 and 5. Lower mass bins systematically require higher \dot{m} for the Comptonized outer disc AGNSED model, while the opposite is true for the highest masses. This is explained by looking in detail for spectra in the black hole mass/luminosities bins highlighted as 1 and 2. *Lower right-hand panel:* In the low-mass bin, the QSOSED UV tied model (red) is dominated by the outer standard disc. A pure standard disc of the same \dot{m} is shown in purple, and has very similar L_{2500} . Comptonizing this entire emission shifts the spectrum to the right (black line), so this has much lower L_{2500} than before. Thus, a fully Comptonized disc requires higher \dot{m} (black dashed line) to recover the same L_{2500} as before. *Upper right-hand panel:* In the high-mass bin, the outer disc peaks below 2500 Å, so the QSOSED UV tied model is dominated by the warm Comptonized emission (red). A pure disc spectrum (purple) at the same \dot{m} has much larger luminosity at 2500 Å. Completely Comptonizing this (black) still has larger luminosity at 2500 Å, so to match the same L_{2500} point requires a smaller \dot{m} .

accretion rates and high masses are predicted to peak at far too low a temperature to make the UV emission seen here. The drop in disc temperature is even more obvious in QSOSED as this has the inner disc progressively replaced by the hot flow as \dot{m} drops (see Fig. 2). Thus, we expect that there should be a clear change in shape for the optical/UV spectra at the same L_{3000} for changing mass (see Fig. 10).

We look for this effect by comparing the spectra at constant L_{3000} for different masses where there are 3 or more mass bins in Fig. 9. These are shown in Fig. A1. Very surprisingly, the optical/UV spectra are almost identical. This is most clearly the case for the highest luminosity bin, $L_{3000} = (45.5-45.75)(\text{erg s}^{-1})$, which contains spectra from four mass bins from $\log(M_{\text{BH}}/M_{\odot}) = (8.0-10.0)$ (shown in Fig. 11 and enclosed in green in Figs 9, A1, B3, and C1). The line widths of H β and MgII clearly show broader line profiles in the higher mass bins, as expected for the change in mass, but the continuum shape shows no significant change.

The Appendix shows that this trend continues for the whole SDSS sample, not just the range covered by the SOUX sample (Fig. B3). It is clear that even in this wider parameter space, the shape of the optical–UV continuum does not vary significantly with M_{BH} at a fixed luminosity. We also check that the same spectral shape is seen in individual objects by comparing our composite spectra with a sample of individual AGN observed by X-shooter (Capellupo

et al. 2015; Fawcett et al. 2022, data by private communication). This instrument covers an extremely wide bandpass, similar to our composites. Fig. C1 shows these composites plotted over the relevant bins from Fig. 11. Again we see no significant differences between any of the spectra across the entire mass range at a given luminosity.

To check that, when measured, the mass of each composite matches the masses of the sources from which each composite was constructed, we fit the composite spectra presented in Fig. 11 with PYQSOFIT and derive a black hole mass for each using the scaling relations of Mejía-Restrepo et al. (2016). The results from this fitting procedure are presented in Table 1. All of the mass estimates fall within the bounds of the mass bin for which each composite was constructed. This allows us to perform detailed fitting of these composite spectra using the central mass of each bin during the fitting procedure.

5.3 Detailed fits to the SDSS composites and fine-tuning

Since we have only the optical/UV spectra, we now go back to the standard (and colour temperature corrected) disc models (Section 3.3 and 3.4) to see if these can fit better to this restricted energy range. We fit disc spectra to this unchanging spectral shape across the M_{BH} range depicted in Fig. 11. This is the approach often taken with individual

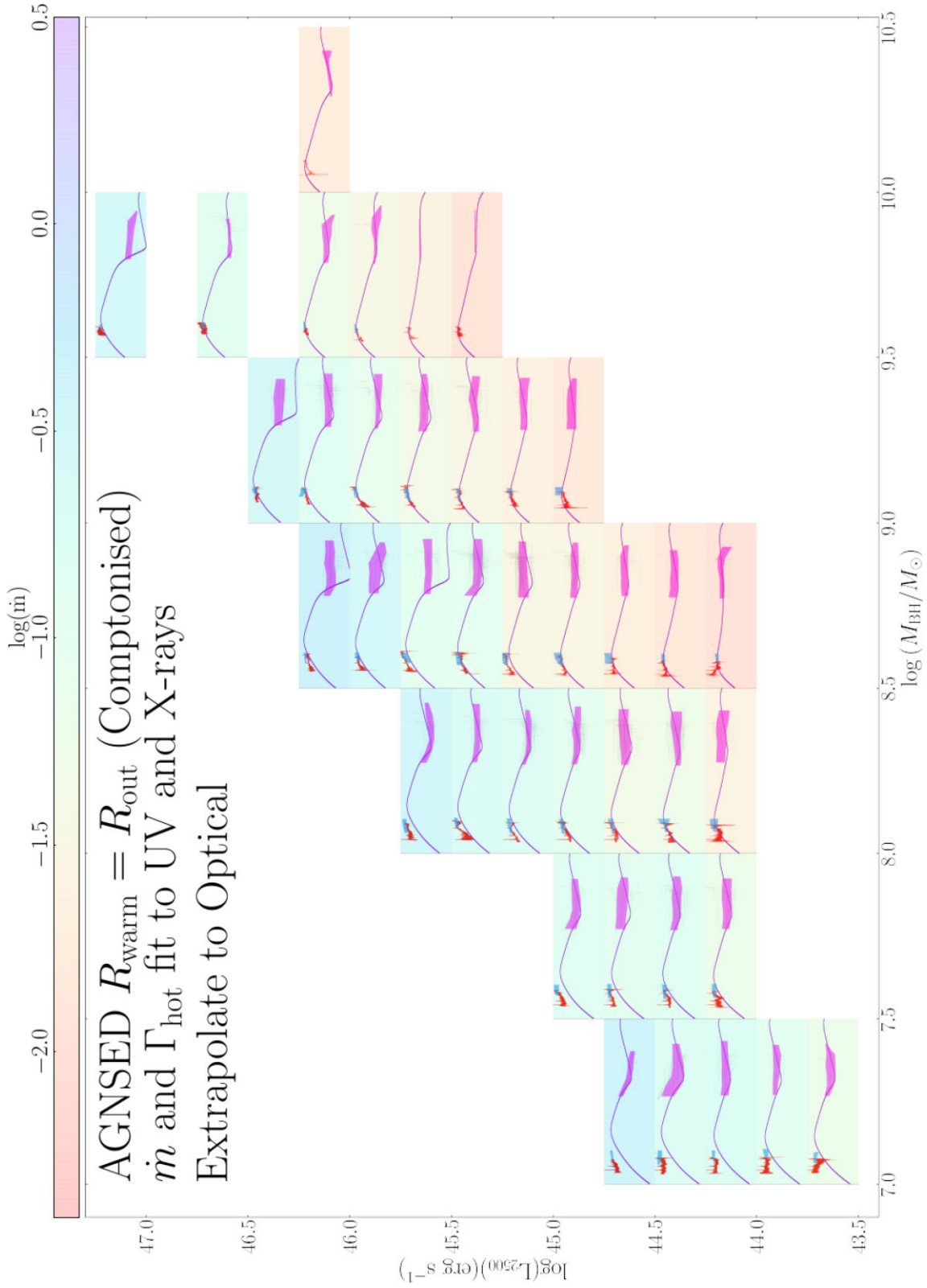


Figure 7. As in Fig. 5 but with the AGNSED model fit to both the UV and X-ray data, allowing R_{hot} and Γ_{hot} to be free parameters in addition to m .

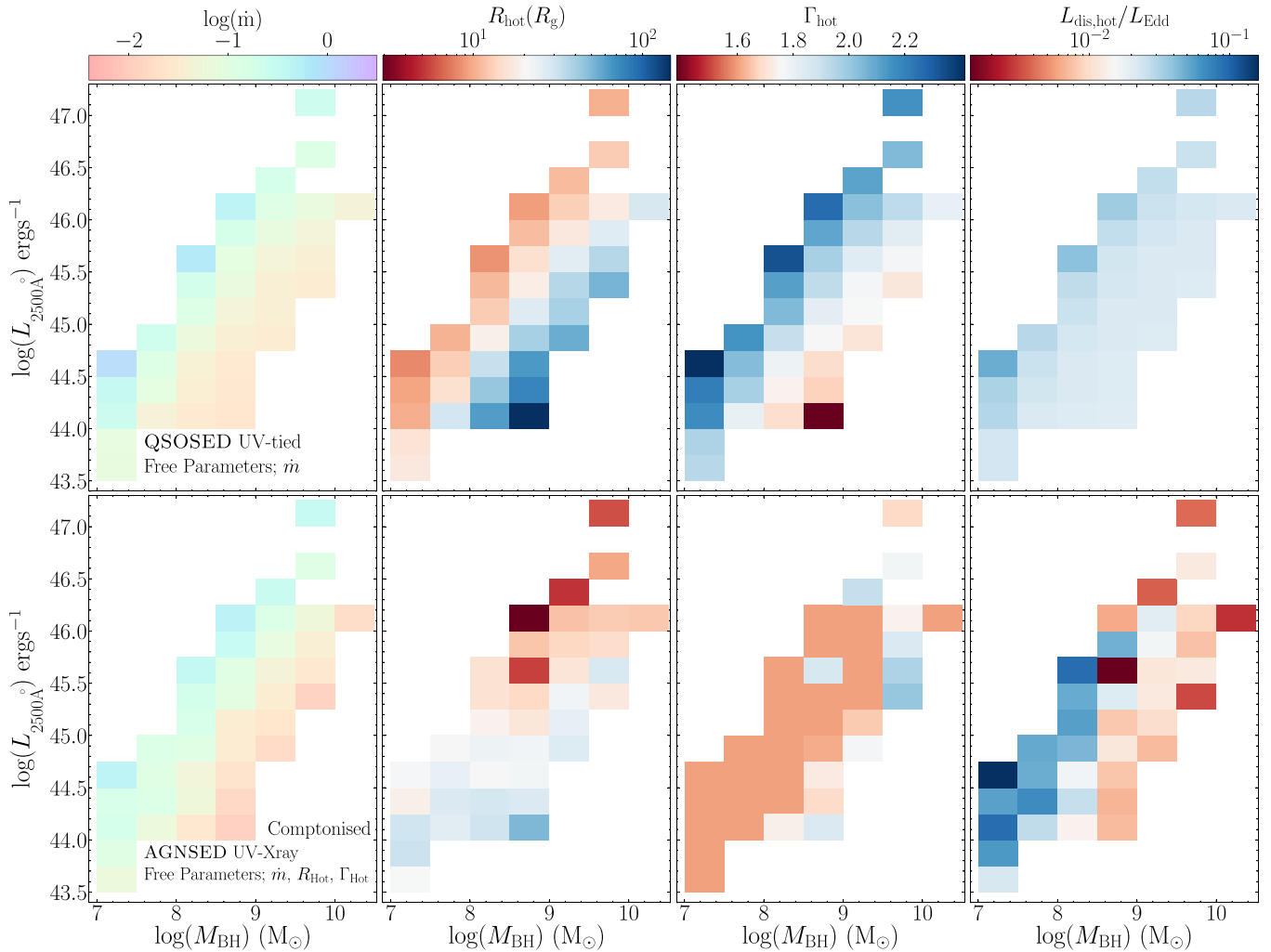


Figure 8. A comparison of the parameters of the QSOSED UV-tied fits (upper panel) and those from the AGNSEd UV-X-ray fits of Fig. 7 (lower panel). Both models have \dot{m} as a free parameter, but the AGNSEd UV-X-ray fits additionally have R_{hot} , Γ_{hot} , and X-ray power, $L_{\text{dis, hot}}/L_{\text{Edd}}$, as free parameters, whereas in QSOSED they are hardwired into the model.

objects, but here we use the composites taken by averaging over many objects, which highlight the fine tuning issues.

5.3.1 Fitting with a_* as a free parameter

First, we explore fitting pure disc models, allowing black hole spin, a_* , to be a free parameter as well as \dot{m} . We take the four mass bins from the $\log(L_{3000}) = (45.5\text{--}45.75)$ (erg s^{-1}) row highlighted in green in Fig. 9 and fit a pure disc model using AGNSEd ($f_{\text{col}} = 1$). It is very clear that highest masses require maximal spin in order to make the disc peak at high enough energy to fit the shortest wavelengths sampled here.

We repeat this with the colour temperature corrected disc, ($f_{\text{col}}(T)$), as incorporated in OPTXAGNF. The same shift to high spin is apparent, but this model now fits the curvature seen in the data, where there is a systematic flattening of the spectra at the shortest wavelengths. This is because the colour temperature correction from electron scattering onset is when the disc temperature exceeds 3×10^4 K. Annuli above this temperature are shifted relative to annuli at lower

temperatures, producing a characteristic bend in the spectrum at a specific wavelength.

It is conceivable that there are real physical mechanisms that cause higher mass black holes to have high spin. However, the fine tuning of a_* and \dot{m} that is necessary to allow the UV-optical continuum shape to remain constant across 2.5 dex in black hole mass, as is shown in Fig. 11, seems contrived.

Additionally, none of these models are self-consistent as while they incorporate general relativistic effects on the intrinsic emissivity (Novikov–Thorne, see Section 3), they do not include relativistic ray tracing on the observed spectrum. There is a strong gravitational redshift expected for high spin, which is much more important than the Doppler blueshift from the fast orbital motion at low inclinations. All these effects are much weaker for low spin. We use RELAGN (Hagen & Done 2023) to incorporate both the general relativistic effects on the emissivity and on the radiation transport to the observer. Fig. 12 shows what happens to the pure disc ($f_{\text{col}} = 1$) and to the colour temperature corrected disc, $f_{\text{col}}(T)$. There is now no adequate fit for the highest mass bin. Increasing black hole spin apparently fit the data as this gave increased high-energy emission by

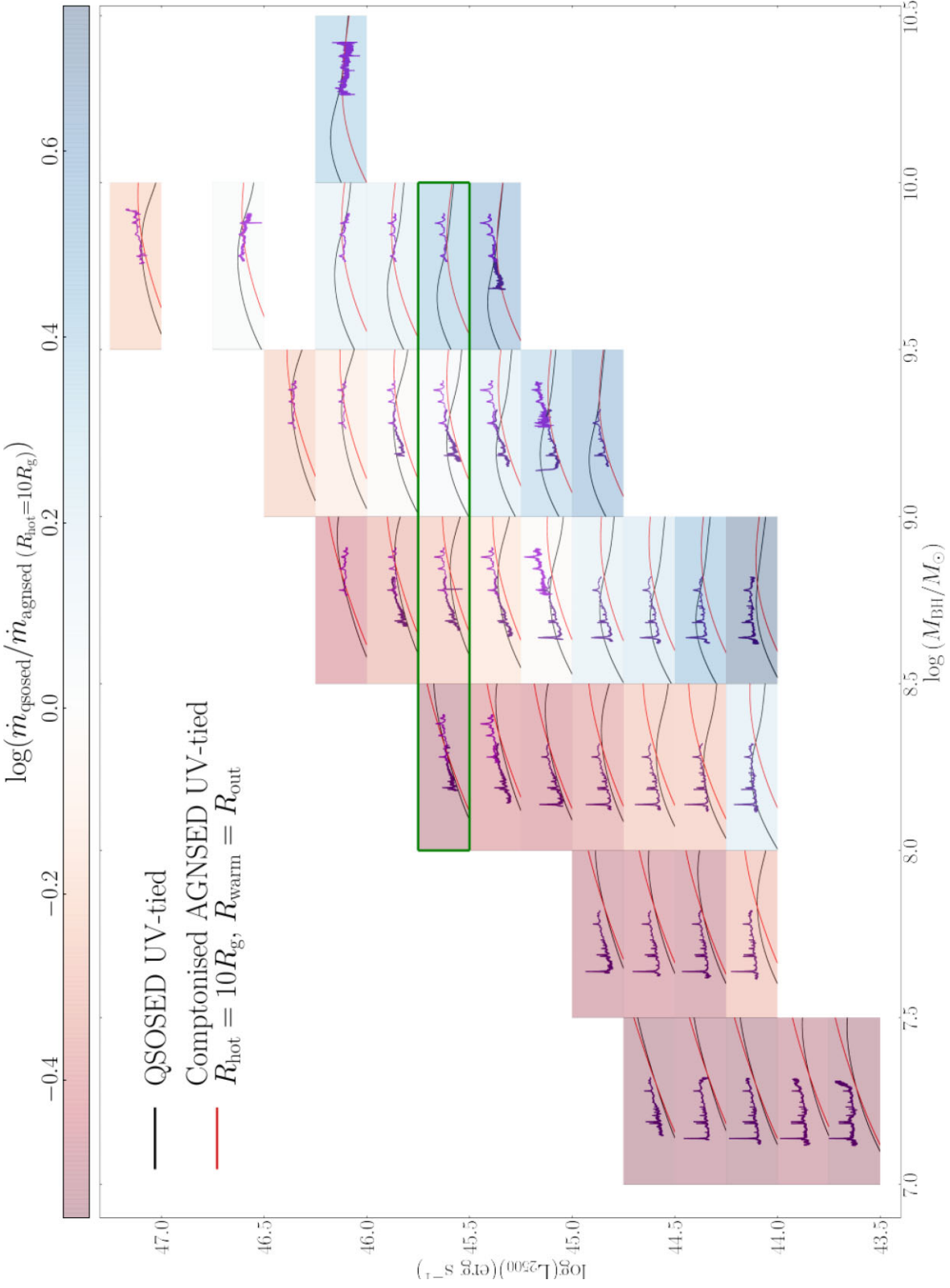


Figure 9. SDSS spectral composites from the full Rakshit DR14 SDSS quasar catalogue (Rakshit et al. 2020) with $z \leq 0.8$ (indigo) and $(2.15 \leq z \leq 2.25)$ (purple). Each bin contains the QSOSED UV-tied SED (black) and AGNSED UV-tied Comptonized SED (red), taken from Figs 4 and 5, respectively. Each bin is coloured on the logarithm of the ratio of m_i 's computed by the QSOSED and the Comptonized AGNSED models. Each of the inset plots span 1.5 dex in luminosity and cover the spectral range between 2×10^{14} Hz and 4×10^{15} Hz.

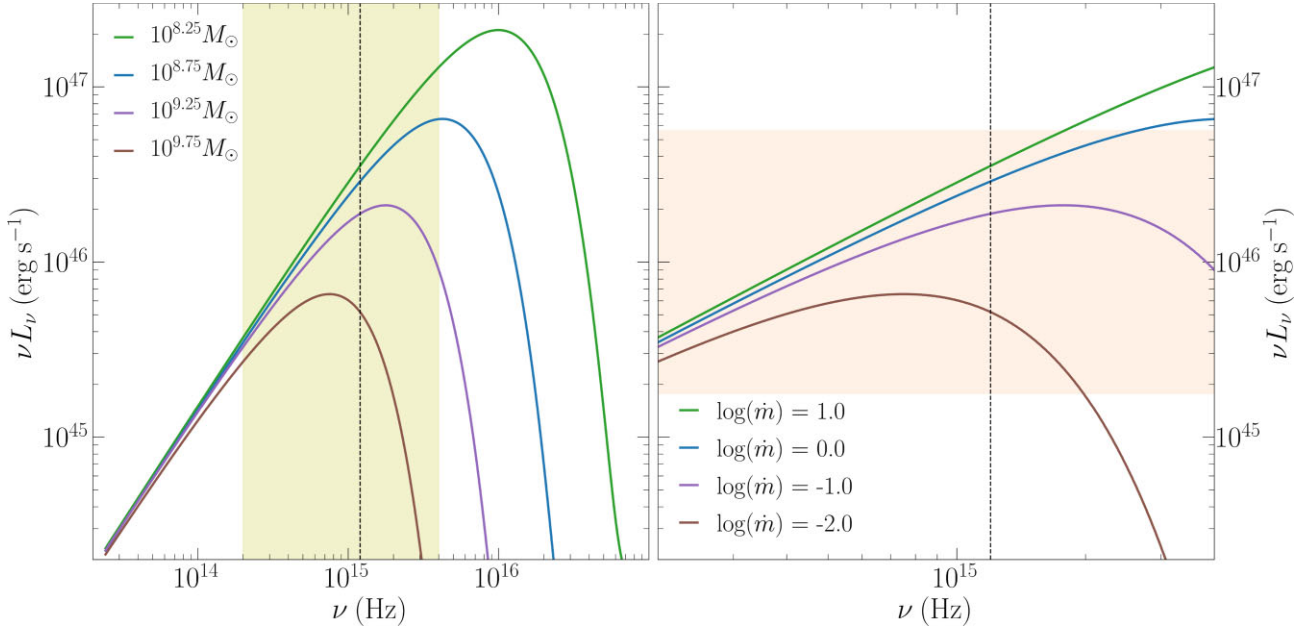


Figure 10. *Left-hand panel:* Pure disc SEDs (spin 0) with M_{BH} centered on the four mass bins enclosed in green in Fig. 9. The spectra are shown over 3 decades in \dot{m} , the necessary range in order to match in Luminosity on the Rayleigh–Jeans tail over a span of 1.5 dex in M_{BH} . However, the spectra clearly peak in the SDSS bandpass (highlighted in yellow), so these do not all have the same L_{2500} . *Right-hand panel:* Zoom-in of the SDSS bandpass, with orange highlighting the range in νL_ν of the insets in Fig. 9. Disc spectra clearly predict that there should be strong evolution in the spectral shape in this range.

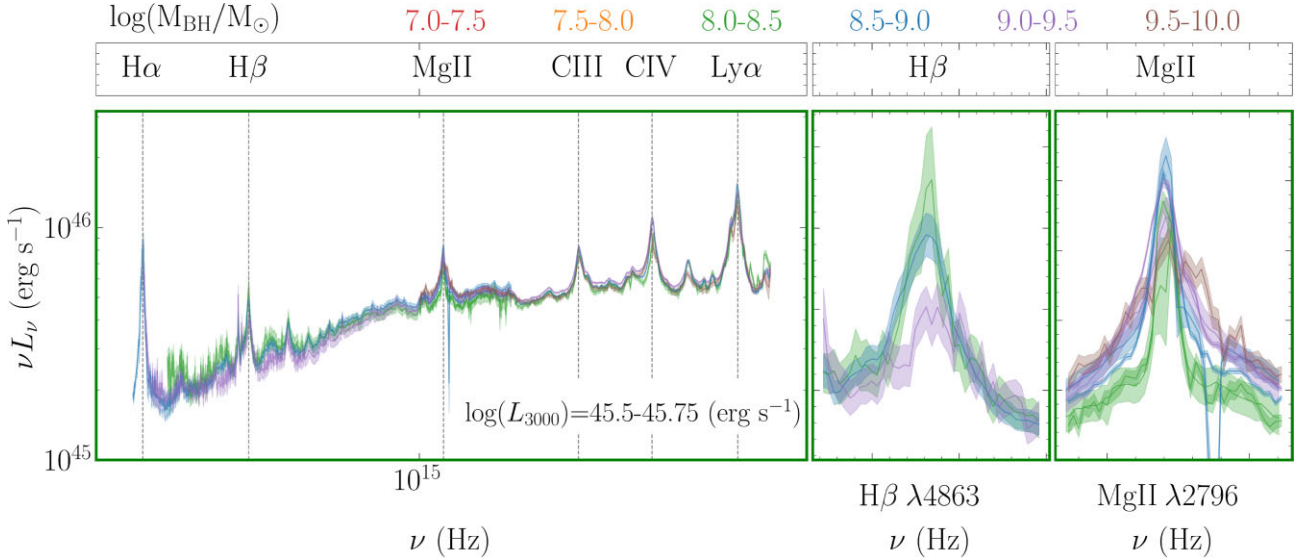


Figure 11. The $L_{3000} = (45.5\text{--}45.75) \text{ erg s}^{-1}$ bin from Fig. 9 showing the unchanging spectral shapes across the mass ranges. The right-hand panels show the $\text{H}\beta$ and Mg II emission-line regions. A separate Mg II profile is shown for both the low and the high z composite in any L_{3000} with overlap.

Table 1. Mass estimates of composite spectra in the $\log(L_{2500}) = (45.5\text{--}45.75) \text{ erg s}^{-1}$ bin, obtained using PYQSOFIT and the scaling relations of Mejía-Restrepo et al. (2016).

$\log(M_{\text{BH}}/M_\odot)$ Range	FWHM (km s^{-1})	$\log(L_{5100})$	Mass (M_\odot)	$\log(M_{\text{BH}}/M_\odot)$
8.0–8.5	2597 ($\text{H}\beta$)	45.36	3.97×10^8	8.47
8.5–9.0	3815 ($\text{H}\beta$)	45.31	5.90×10^8	8.77
9.0–9.5	6610 ($\text{H}\beta$)	45.32	1.80×10^9	9.25
9.5–10.0	8161 (Mg II)	45.61	5.53×10^9	9.74

decreasing the inner disc radius but these smallest radii are the most affected by gravitational redshift, offsetting all the gain in far UV emission.

We also fit these four disc regimes allowing for intrinsic reddening as a free parameter using the XSPEC model ZDUST. The resultant $E(B - V)$ values are only significant for the lowest two mass bins of $\log(M_{\text{BH}}/M_\odot) = (8.0\text{--}8.5)$ and $\log(M_{\text{BH}}/M_\odot) = (8.5\text{--}9.0)$ and for the pure disc ($f_{\text{col}} = 1$) for the $\log(M_{\text{BH}}/M_\odot) = (9.0\text{--}9.5)$. For all other disc regimes and for all of the disc regimes in the highest mass bin $\log(M_{\text{BH}}/M_\odot) = (9.5\text{--}10.0)$, the resultant $E(B - V)$ values are

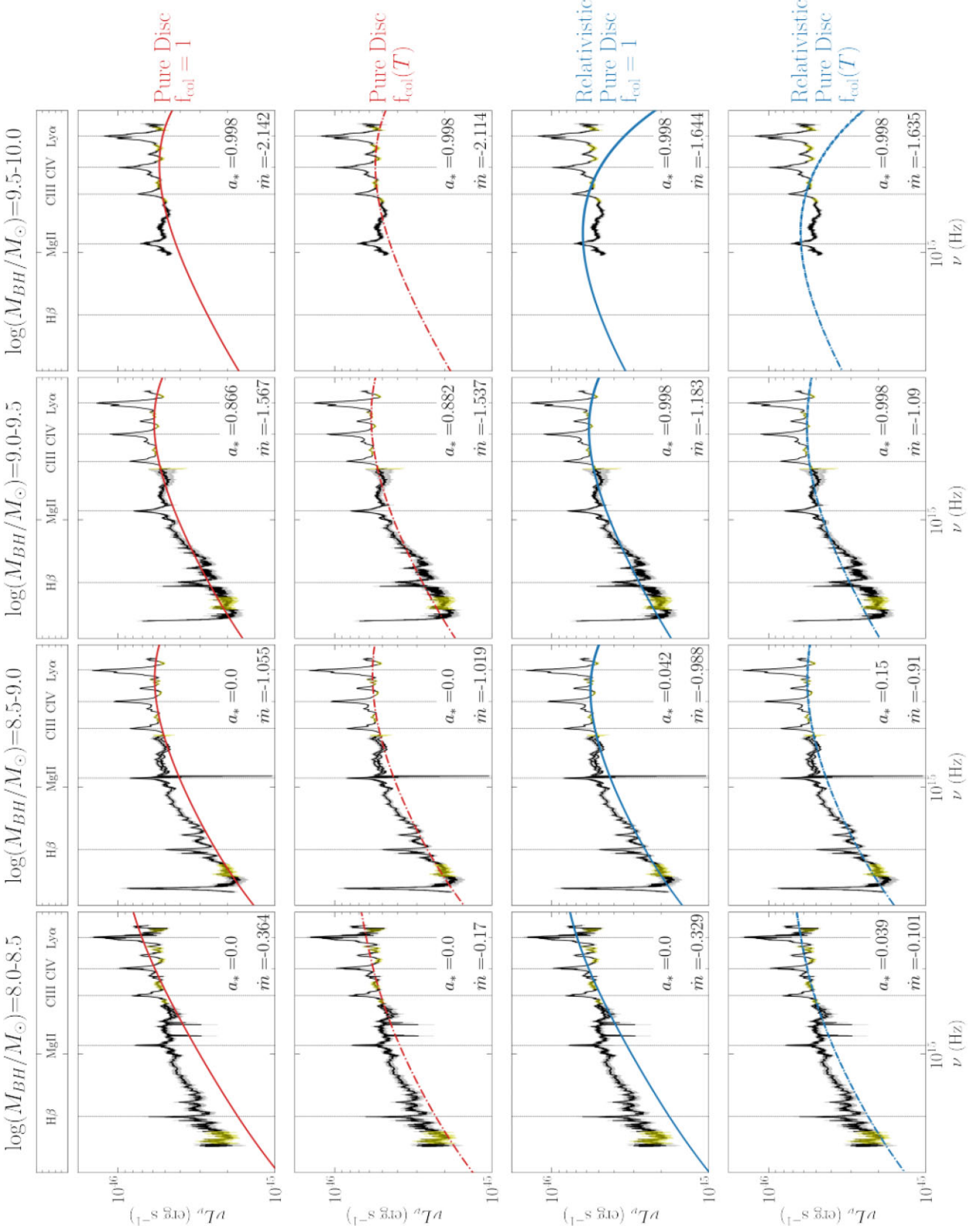


Figure 12. Four mass bins, taken from Fig. 9, of constant mean $\log(L_{3000}) = (45.5-45.75)(\text{erg s}^{-1})$, spanning 2 dex in $\log(M_{\text{BH}}/M_{\odot})$ from 8.0 to 10.0, fit with AGNSD, OPTXAGNF, RELAGN, and RELAGNF, where RELAGNF is RELAGN with a colour temperature correction applied. Each model was fit for \dot{m} and a_* to the clean continuum regions highlighted in yellow, the resultant value of which are displayed on each panel.

insignificant. This strongly indicates that intrinsic reddening does not help in fitting disc spectra to the optical-UV continua of high mass AGN. This is as expected as the high-mass spectra are far more blue than predicted by the disc models.

5.3.2 Fitting a standard disc with minimal and maximal spin

We illustrate the issues above by plotting the models over a wider energy range for the highest and lowest mass bins. Fig. 13 shows a comparison of minimal and maximal spin models for the four disc models shown in Fig. 12 for the $\log(M_{\text{BH}}/M_{\odot}) = (8.0-8.5)$ and $\log(M_{\text{BH}}/M_{\odot}) = (9.5-10.0)$ mass bins at fixed $\log(L_{3000}) = (45.5-45.75)$ (erg s^{-1}).

In the lower mass bin of $\log(M_{\text{BH}}/M_{\odot}) = (8.0-8.5)$ all four disc models are able to give a reasonable fit to the spectral shape of the optical-UV continuum. In this mass range, with $a_* = 0$, the relativistic correction makes very little difference to the SED shape, the colour temperature correction has far more impact and shifts the peak to higher energies in a similar fashion to Comptonization. Here, the colour temperature corrected fits, dashed lines, provide a better overall fit to the data, and have lower \dot{m} values.

When a_* is fixed at 0.998, maximal spin, the colour temperature corrected models again show better fits to the data. However, the overall spectral shape of the SED is greatly changed, with the relativistic corrections having a much greater effect than the colour temperature correction. The effect of having maximal spin is to drag the peak of emission to much higher energies, this is significantly counter acted however when general relativity is taken into account and the peak of emission is shifted towards lower energies. This occurs due to the increased importance of relativistic redshift on the emission as opposed to blue shift at high spin, whereas at low spin these factors are much more balanced.

At high mass the picture is very different. With $\log(M_{\text{BH}}/M_{\odot}) = (9.5-10.0)$ and $a_* = 0$, the SED shape for all four disc regimes is almost identical, and plainly does not match the data. At these high masses and zero spin, general relativity has almost no effect, other than to slightly increase the \dot{m} value for a given L_{3000} . A common approach at these masses is to assume high spin. The bottom right-hand panel of Fig. 13 shows that a pure disc at maximal spin, with or without a colour temperature correction matches the spectral shape of the high-mass composite well. However, once general relativity is taken into account, all that is gained in shifting the peak to higher energies by maximizing spin is lost again, as the peak of emission shift back to lower energies and once again does not fit the data well.

This shows clearly that there is no way to make the optical/UV spectra seen from the highest mass AGN from a standard (or colour temperature corrected) disc for these masses and mass accretion rates. Even if all the energy is dissipated in a disc (with the hard and soft X-rays powered by e.g. a separate coronal flow or by tapping the spin energy of the black hole) the UV emission extends to higher energies than predicted for the accretion disc peak in full general relativity (Figs 12 and 13).

5.3.3 Fitting a fully Comptonized disc with minimal and maximal spin

A blackbody disc cannot fit the highest masses, even with colour temperature correction as expected from a standard disc photosphere. Instead, we explore the viability of fitting fully Comptonized disc spectra, as suggested by Petrucci et al. (2018), which implies that the energy is dissipated away from the mid-plane, towards the

photosphere. Since the SDSS data do not cover the soft X-ray excess, we fix its electron temperature at 0.2 keV.

We fit a fully Comptonized disc ($R_{\text{warm}} = R_{\text{out}}$, $R_{\text{hot}} = R_{\text{isco}}$) for \dot{m} with $\Gamma_{\text{warm}} = 2.5$, and a Comptonized pure disc fit with both \dot{m} and Γ_{warm} as free parameters, to the $\log(M_{\text{BH}}/M_{\odot}) = (8.0-8.5)$ and $\log(M_{\text{BH}}/M_{\odot}) = (9.5-10.0)$ bins, at fixed $L_{3000} = (45.5-45.75)$ (erg s^{-1}). We repeat this process for the same disc models but with the addition of full general relativity. The results of this fitting process are shown in Fig. 14.

In the low-mass regime, both at zero and maximal spin, the optical-UV continuum shape of the composite is too red to fit well to any of the Comptonized disc spectra. The inclusion of general relativity does not make a difference to the fit to the data; however, it does change the overall shape of the SED and reduces L_{bol} dramatically. The same is true when fitting to Γ_{warm} , which in both the zero and maximal spin regimes results in the maximum allowed value of $\Gamma_{\text{warm}} = 3.5$.

In the high mass bin, Comptonization provides a better fit to the data. In the spin zero models, there is very little difference between the Comptonized pure discs with and without general relativity, and the best-fitting Γ_{warm} pegs at the minimum value of 2.1 though there is more dispersion for the Comptonization shape at high spin.

Comptonization does not solve all the issues, there is clearly a need for Γ_{warm} to change as a function of M_{BH} or perhaps more likely physically with \dot{m} . However, it does at least allow the models to fit to the furthest UV emission observed in the data. The key issue is our (lack of) understanding of the physics which sets this emission component.

6 THE STRUCTURE OF THE ACCRETION FLOW

The QSOSED model is a good zeroth-order predictor of the intrinsic AGN spectrum (Fig. 4). In particular, it is clear that the assumptions made about the hot Comptonization region match fairly well to the X-ray luminosity and spectra seen in the 2–10 keV bandpass across most of the range of mass and \dot{m} in our sample. This favours the underlying assumption that the hot corona dissipates up to the ADAF maximum of $L_{\text{diss}} = 0.02L_{\text{Edd}}$. For accretion flows below this limit, the entire accretion power is dissipated in the hot corona rather than in a UV bright disc. This means there is no longer a strong UV ionizing flux so no strong BLR, leading to an optical classification as an LINER or true type-2 Seyfert. This gives the observed mass dependence of the lowest luminosity spectra identified as QSOs in SDSS.

The outer disc extends inwards as the source luminosity increases above the ADAF limit, but unlike the stellar mass BHB at the same L/L_{Edd} , the disc is still truncated so that there is substantial hard X-ray power with $L_{\text{diss}} = 0.02L_{\text{Edd}}$. In the QSOSED model, this requirement sets the extent of truncation of the optically thick material, R_{hot} . The inner disc only extends down close to the ISCO for $L \gtrsim 0.1L_{\text{Edd}}$, giving the changing fraction of disc to X-ray power seen in the data.

Similarly, the warm Comptonization region in QSOSED is a fairly good match to the soft X-ray/UV data at zeroth-order despite the assumptions underlying this component being completely phenomenological. In particular, the assumption that the radius of the warm Comptonization region is $R_{\text{warm}} = 2R_{\text{hot}}$ means that the extent of this component is limited at high L/L_{Edd} where $R_{\text{hot}} \sim R_{\text{isco}}$, whereas it covers most of the outer disc at $L/L_{\text{Edd}} \sim 0.02$. The condition $R_{\text{warm}} = 2R_{\text{hot}}$ equivalent to assuming that the soft Comptonization carries a more or less fixed fraction of the bolometric luminosity, with $L_{\text{warm}} = 0.2L_{\text{bol}}$.

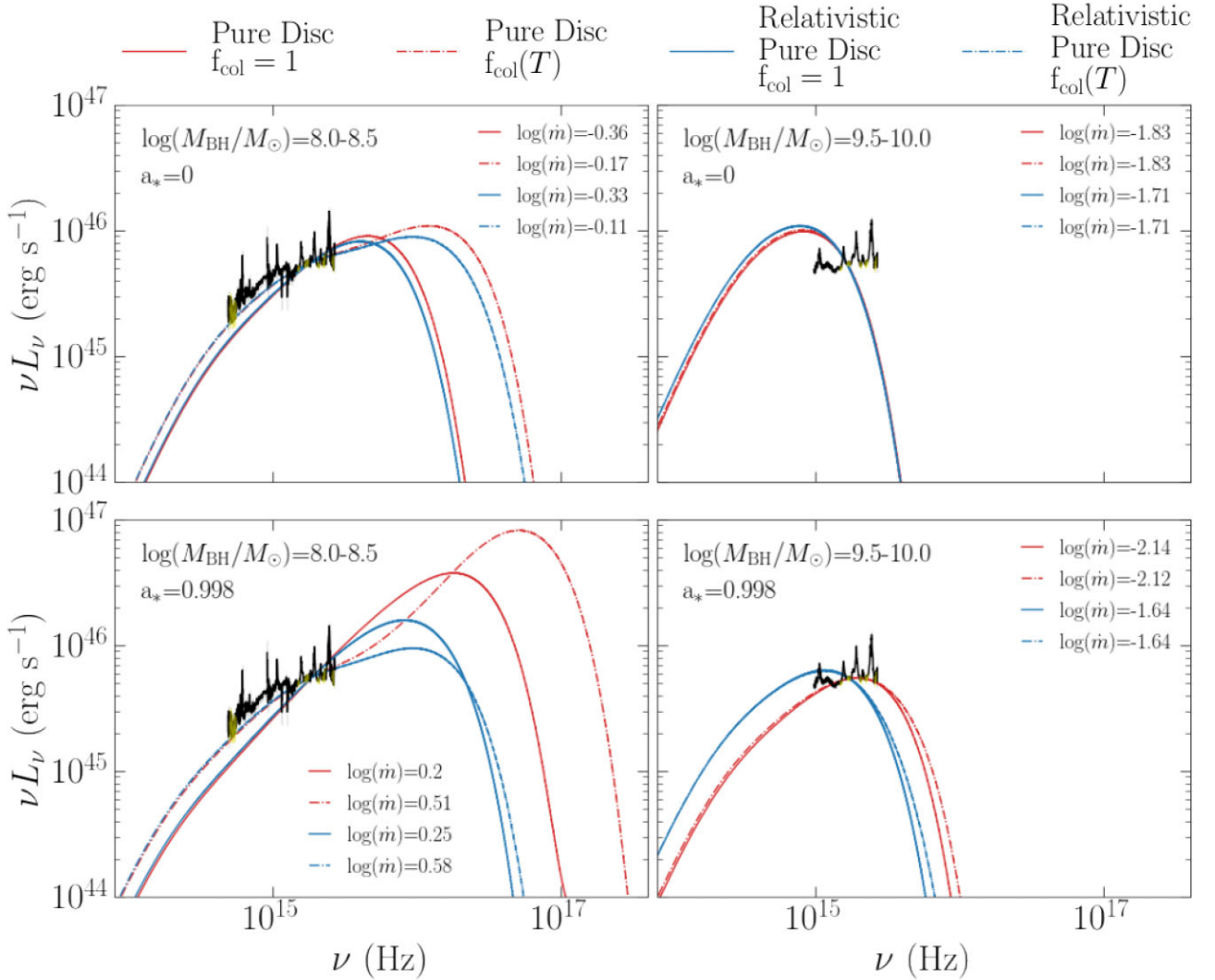


Figure 13. The SDSS composites for constant $\log(L_{3000}) = 45.5\text{--}45.75$ (erg s^{-1}) for mass of $\log(M_{\text{BH}}/M_{\odot}) = (8.0\text{--}8.5)$ (left) and $\log(M_{\text{BH}}/M_{\odot}) = (9.5\text{--}10.0)$ (right). Yellow points indicate the continuum dominated regions used for the fits. Models are a pure disc (red solid), colour temperature corrected disc (red dashed). The blue solid and dashed lines indicate the same models but with the self-consistent ray tracing. This does not have a large effect for spin 0 (upper panels), but is very important for high spin (lower panel), where gravitational redshift means that no disc model with dissipation in the mid-plane can fit the data.

The QSOSED component which is the worst fit is the one which is best motivated physically, namely the standard disc emission assumed for the outer radii. For the highest masses, and lowest luminosities, the disc temperature should result in a peak below 1200 \AA even for an untruncated disc, let alone the quite strongly truncated disc assumed by QSOSED at low L/L_{Edd} . This mismatch is present in the literature but is disguised as individual objects seem fairly well fit using extreme black hole spin. This gives a higher temperature disc peak from the smaller R_{isco} size scales. However, these models only incorporated the effects of general relativity on the disc emissivity (Novikov–Thorne, as used here), but did not include its effect on ray tracing from the disc to the observer (Capellupo et al. 2016). There is gravitational and transverse red shift that depends on R , whereas the Doppler red and blue shifts from orbital motion depend on both R and inclination. These shifts are generally negligible for the optical/UV spectra of QSO with masses $\lesssim 10^9 M_{\odot}$, as the radii emitting these wavelengths are at $R \gtrsim 10R_g$. However, for the most massive QSO the observed UV is produced close to R_{isco} . Pure disc models with low spin do not have sufficiently high temperatures to match the observed

UV. High spin models appear able to do this as the intrinsic disc temperature is higher when including the additional inner disc radii from $R = (6\text{--}1.23)R_g$. However, this higher temperature emission is strongly gravitationally redshifted on its way out to the observer, which reduces the observed temperature back to something close to the low spin disc models.

Pure disc models are then not able to match the observed outer disc emission at the highest masses once the self-consistent ray tracing is included. Either the masses are wrong, or the standard disc models are wrong (or both). We examine each of these in turn below.

6.1 Changes to the standard disc emission

We saw above that the models where the entire outer disc emitted a warm Comptonization spectrum rather than (colour temperature corrected) blackbody enabled the accretion power to reach the highest UV energies observed. However, it requires a correlation of Γ_{warm} with L/L_{Edd} , such that the lowest L/L_{Edd} AGN have hardest $\Gamma_{\text{warm}} \sim 2$ while the highest L/L_{Edd} have $\Gamma_{\text{warm}} \sim 3.5$. This is certainly supported

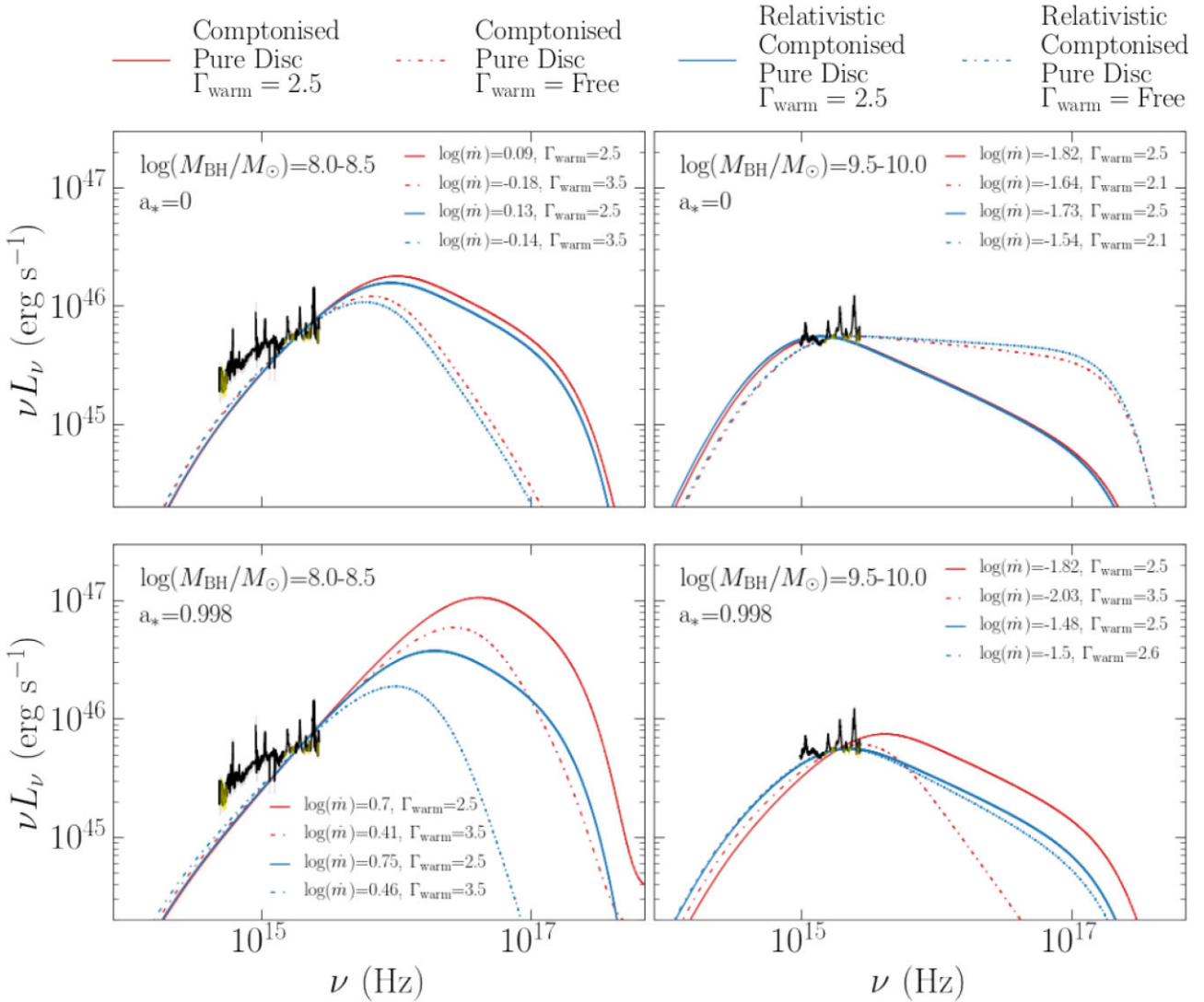


Figure 14. The same as Fig. 13, but with Comptonized disc models. The solid red lines have $\Gamma_{\text{warm}} = 2.5$ (as in QSOSED), while the red dashed lines have Γ_{warm} as a free parameter. Again, models in blue include the self-consistent ray tracing.

from observational data, as multiple high L/L_{Edd} NLS1 show $\Gamma_{\text{warm}} \sim 3.5$ and this can be produced in the theoretical models when the underlying disc is not purely passive (Petrucci et al. 2018). However, this is completely dependent on the unknown structure of the warm Comptonization region, and detailed models require much more understanding of this regime. None the less, the warm Comptonization models are the only disc based spectra that can match the data from the highest mass QSO at lower luminosity.

Alternatively, the accretion structure could be completely different to that expected from a disc. We based even our non-standard disc models on the standard Novikov–Thorne emissivity that assumes that the α viscosity remains constant across the disc. Yet it is starting to become clear that hydrodynamic convection couples to the magnetic dynamo, strengthening the heating in convectively turbulent regions (Jiang, Guillochon & Loeb 2016b; Jiang & Blaes 2020). Hydrodynamic convection could be triggered by the strong bumps in opacity at 10^4 K from H, $10^{4.6-4.8}$ K from He and $10^{5.2}$ K from iron (a blackbody at 10^4 peaks at 3000 \AA). Massive stars have similarly bright UV emission, and these also show strong winds, powered by UV line driving, as well as turbulent

convection triggered by the continuum UV opacity (Jiang et al. 2015; Ro 2019). Alternatively, convection could be triggered by the radiation pressure instability. This becomes more dominant at highest $\log(M_{\text{BH}}/M_{\odot})$ though the expected dependence is rather slow, with $R_r/P_g = 7.3 \times 10^9 m_{\odot}^{1/4} \dot{m}^2 \alpha^{1/4} r^{-21/8}$.

Either warm Comptonization of the outer disc, or a different accretion structure potentially can work by shifting the emission to higher temperatures, so it peaks in the unobservable EUV part of the spectrum. The observed UV/optical emission is instead produced by re-processing of this EUV peak from dense material. The BLR must subtend a substantial solid angle, and dense clouds within the BLR can give a diffuse continuum (Korista & Goad 2001; Cackett et al. 2018; Korista & Goad 2019). There is also growing evidence for a dense clumpy wind on the inner edge of the BLR which again produces predominantly diffuse continuum (free-free and bound-free rather than lines; Kaastra et al. 2014; Miniutti et al. 2014). A predominantly reprocessed origin for the optical/UV is the easiest way to explain its remarkably constant shape, as well as fitting in with the longer timescale lags seen in the continuum reverberation intensive monitoring campaigns.

Table 2. Three single epoch virial black hole mass estimates calculated using spectra taken from Boroson & Green (1992), Buttiglione et al. (2009), and Torrealba et al. (2012), along with the measurement from Gravity Collaboration et al. (2018).

Source	Mass (M_{\odot})
Boroson & Green (1992)	6.79×10^8
Buttiglione et al. (2009)	1.22×10^9
Torrealba et al. (2012)	2.51×10^8
Gravity Collaboration et al. (2018)	$(2.6 \pm 1.1) \times 10^8$

6.2 Testing black hole masses

The unexpectedly constant shape of the optical–UV continuum that we observe could potentially indicate that the mass scaling relations are inaccurate at high M_{BH} . We test the robustness of the single epoch virial mass estimates at high black hole masses using single epoch spectra from 3C273, comparing them to the mass derived from the independent method of spatially resolving the broad-line region (Gravity Collaboration et al. 2018). We obtained three independent optical spectra of 3C273 spanning 20 yr from Boroson & Green (1992), Buttiglione et al. (2009), and Torrealba et al. (2012). We use the PYQSOFIT software package to measure the FWHM of the H β line profile, and the 5100 Å continuum luminosity, and derive mass from the scaling relations of Mejía-Restrepo et al. (2016) as for the SOUX AGN sample. These results are shown in Table 2 and show a spread of 0.69 dex, with a mean mass which is higher than the Gravity result. Thus, there could be a systematic overestimate of black hole mass, which could shift a source up between 1 and 2 of our 0.5 dex bins. This could give a systematic effect as there are many more lower mass black holes than high mass ones, so numbers scattered to higher masses are not compensated by number of higher mass objects scattered down (e.g. Davis, Woo & Blaes 2007).

However, the constant shape of the optical-UV continuum is observed across 1.5–2 dex (4 bins) in M_{BH} in the SOUX sample (see Fig. 11) and 2–2.5 dex (5 bins) in M_{BH} in the wider SDSS parameter space (see Fig. B1). This would require an extremely large systematic shift in the mass estimation that seems unlikely given the number of sources used in the creation of the composite spectra. Such a shift would have consequences for all black hole mass estimates.

Based on this preliminary study, it is possible that there is a systematic overestimation of M_{BH} at high masses, but this is not likely to be large enough to be the dominant factor causing the homogeneous optical-UV continuum shape that we observe. As the number of AGN with a spatially resolved broad-line region increases, a more robust test of single epoch virial black-hole mass estimates will hopefully become possible.

Aside from the possibility that the scaling relations are inaccurate, the M_{BH} values that we adopt from R20 could be contaminated, particularly where Mg II is utilized. This seems unlikely however, given that R20 perform a subtraction of the UV Fe II emission by fitting a velocity-broadened template, and that we perform a S/N cut. Even if a systematic overestimation in M_{BH} due to some kind of contamination existed in the masses quoted by R20, it would doubtful be large enough to cause the shape of the optical-UV continuum to remain constant over 2–2.5 dex.

For the SOUX sample, there is a ≈ 60 per cent overestimation in the Mg II masses with respect to H β masses in sources with both lines present. These masses were calculated in K23 using the scaling relations from Mejía-Restrepo et al. (2016). This only corresponds

to 0.2 dex, an offset of too small a magnitude to cause the effect we see over 2–2.5 dex in M_{BH} .

7 SUMMARY AND CONCLUSIONS

We demonstrate the advantages of studying a sample large enough to investigate population statistics, but based on available high-quality multiwavelength data. This enables us to carry out detailed SED analysis over a wide parameter space rather than for individual objects.

We stack spectra from our sample on a 2D grid in M_{BH} and L_{2500} . All AGNs in a single grid point should have the same black hole mass range and mass accretion rate (including uncertainties in black hole mass estimates, and inclination angle) so that their spectra can be averaged with confidence that the objects are similar. We compare the stacked SED in each grid point with the recent AGN SED model of KD18, QSOSED. This model consists of an inner hot flow with fixed X-ray heating of $L_x = 0.02L_{\text{Edd}}$ (the maximum ADAF luminosity). This condition determines the inner radius of the optically thick disc, R_{hot} , and thermalization is assumed to be incomplete out to $R_{\text{warm}} = 2R_{\text{hot}}$, making the soft X-ray excess connect to the UV downturn from warm Comptonization, before thermalizing to a blackbody from R_{warm} to R_{sg} .

To a reasonable degree, the model in each grid box matches well the observed stacked SED across the entire range of mass accretion rates for intermediate masses $\log(M_{\text{BH}}/M_{\odot}) = 7.5\text{--}9.0$. This is despite it not being fit to the optical or X-ray data. This is quite strong evidence that the underlying assumptions in QSOSED are a fairly good description of the accretion flow, although to first order the X-ray flux is underpredicted by a factor of 2 at the lowest M_{BH} . However, at the highest masses, $\log(M_{\text{BH}}/M_{\odot}) > 9$, there is a clear discrepancy in the shape of the optical-UV continuum predicted by the QSOSED models. This is very surprising, as this is the part of the spectrum dominated by the thermal disc, which is the part of QSOSED which has a solid theoretical basis. Instead, we remove the thermalized outer disc, so that all of the optically thick disc emission emerges as warm Comptonization. This component is poorly understood, so we first use the same parameters as in QSOSED, ($\Gamma_{\text{warm}} = 2.5$, $kT_{\text{e,warm}} = 0.2$ keV) and fix $R_{\text{hot}} = 10$ (equivalent to $L_x = 0.07 L_{\text{bol}}$). This gives a much better fit to the optical-UV continuum at high mass, but now does not match well the lower mass bins which were well fit with an outer standard disc. Allowing R_{hot} to vary does not improve the fits. There is a systematic shift between any disc model (warm Comptonized or thermal blackbody) and the optical-UV spectrum. Either the low M_{BH} can be fit with a thermal outer disc, which misses the high M_{BH} , or the high M_{BH} can be fit with a warm Comptonized disc, which misses the low M_{BH} .

We examine this shift in more detail by constructing wide wavelength coverage composite SDSS spectra for each of the SOUX AGN sample grid points. We combine together optical (low redshift) quasar spectra, with mass from H β and UV (higher redshift) quasar spectra with mass from Mg II to produce a stacked spectrum in each grid point of $\log(M_{\text{BH}}/M_{\odot})$ and L_{3000} . These optical-UV composites are of higher quality than the original SOUX SDSS-OM composites as the UV is now based on spectra rather than photometry. They show the same shift with respect to the thermal or Comptonized disc models (Fig. 9). However, from these spectra we now clearly see that the SED peak shift is present in the models, but is not seen in the actual data. Furthermore, at a given luminosity the SDSS stacked spectra remain remarkably constant as a function of M_{BH} (Fig. 11). All disc models are based on a size scale of the inner disc, irrespective of whether it is Comptonized or not, and this size scale increases as M_{BH}

increases. This decreases the inner disc temperature until it peaks in the observable UV bandpass for the highest M_{BH} in our sample. (Fig. 10). But the data show no sign of this predicted change (Fig. 11). We demonstrate this by fitting the pure blackbody disc models to spectra at constant L_{3000} across four different mass bins (Figs 12 and 13). The only way to maintain the constant continuum shape is to systematically increase the spin so as to move the expected peak disc temperature above the UV bandpass. While there could conceivably be a physical connection between the most massive black holes and their spins (e.g. Volonteri, Sikora & Lasota 2007; Fanidakis et al. 2011; Griffin et al. 2019; Huško et al. 2022) this requirement seems to be fine-tuned, especially as we use stacked spectra rather than single objects. More fundamentally, such models are not self-consistent as they only incorporate spin on the intrinsic disc emissivity, but do not include the general relativistic effects of ray tracing from the origin in the disc to the observer. Increasing the spin can succeed in fitting the highest mass spectra as it reduces the size scale of the inner disc, thereby increasing the peak temperature. But this is significantly compensated by the increased gravitational redshift of the emission and so the high spin models cannot fit the UV data.

We explore whether this could be due to mass estimates being systematically biased so that M_{BH} is overestimated at high M_{BH} . However, while this is possible, it seems unlikely to account for the magnitude of the effect we find. Therefore, we consider that it is more likely the accretion structure is different than that shown by thin disc models, such that the ‘disc’ always peaks in the EUV bandpass, even at the highest black-hole masses. Reprocessing of this EUV component then gives the constant shape of the optical/UV spectrum (see also Lawrence 2018 for the same idea based on variability).

One possible way to do this is if the outer disc is completely covered by warm Comptonizing material. But this also requires that the spectral index Γ_{warm} increases with L/L_{Edd} , perhaps indicating a larger fraction of power is dissipated in the disc itself.

Instead, there could be a more fundamental change in the accretion flow if the dissipation always peaked in the EUV region, perhaps due to magneto-rotational instability coupling to the hydromagnetic turbulence generated by sharp changes in the opacity (Coleman et al. 2016; Jiang, Davis & Stone 2016a; Coleman et al. 2018; Jiang & Blaes 2020). We will explore these ideas further in subsequent papers.

ACKNOWLEDGEMENTS

J A J Mitchell and S Hagen acknowledge the support of the Science and Technology Facilities Council (STFC) studentship ST/S505365/1 and S Hagen acknowledges the support of STFC studentship ST/V506643/1. C Done and M J Ward acknowledge support from STFC grant ST/T000244/1. M J Ward acknowledges an Emeritus Fellowship award from the Leverhulme Trust. H Landt acknowledges a Daphne Jackson Fellowship sponsored by the STFC. This research has made use of the NASA/IPAC Infrared Science Archive, which is funded by the National Aeronautics and Space Administration and operated by the California Institute of Technology. D Kynoch acknowledges support from the Czech Science Foundation project no. 19-05599Y, funding from the Czech Academy of Sciences, and the receipt of a UK STFC studentship ST/N50404X/1. Many thanks to Vicky Fawcett for providing X-Shooter data through private communication.

We acknowledge James Matthews and Matthew Temple for constructive conversations and for providing insights into their interesting data set and analysis. We also thank Matteo Monaco for his Masters project work on stacking SDSS spectra which showed the feasibility of this approach.

Funding for the SDSS-IV has been provided by the Alfred P. Sloan Foundation, the U.S. Department of Energy Office of Science, and the Participating Institutions. SDSS-IV acknowledges support and resources from the Center for High-Performance Computing at the University of Utah. The SDSS web site is www.sdss.org.

SDSS-IV is managed by the Astrophysical Research Consortium for the Participating Institutions of the SDSS Collaboration including the Brazilian Participation Group, the Carnegie Institution for Science, Carnegie Mellon University, the Chilean Participation Group, the French Participation Group, Harvard-Smithsonian Center for Astrophysics, Instituto de Astrofísica de Canarias, The Johns Hopkins University, Kavli Institute for the Physics and Mathematics of the Universe (IPMU)/ University of Tokyo, the Korean Participation Group, Lawrence Berkeley National Laboratory, Leibniz Institut für Astrophysik Potsdam (AIP), Max-Planck-Institut für Astronomie (MPIA Heidelberg), Max-Planck-Institut für Astrophysik (MPA Garching), Max-Planck-Institut für Extraterrestrische Physik (MPE), National Astronomical Observatories of China, New Mexico State University, New York University, University of Notre Dame, Observatório Nacional/MCTI, The Ohio State University, Pennsylvania State University, Shanghai Astronomical Observatory, United Kingdom Participation Group, Universidad Nacional Autónoma de México, University of Arizona, University of Colorado Boulder, University of Oxford, University of Portsmouth, University of Utah, University of Virginia, University of Washington, University of Wisconsin, Vanderbilt University, and Yale University.

This research has made use of data obtained from the 4XMM *XMM-Newton* serendipitous source catalogue compiled by the 10 institutes of the *XMM-Newton* Survey Science Centre selected by ESA.

This research made use of *ASTROPY*,¹ a community-developed core PYTHON package for Astronomy (Astropy Collaboration et al. 2013, 2018).

DATA AVAILABILITY

The data underlying this article will be shared on reasonable request to the corresponding author.

REFERENCES

- Abramowicz M. A., Czerny B., Lasota J. P., Szuszkiewicz E., 1988, *ApJ*, 332, 646
- Alexander D. M. et al., 2003, *AJ*, 125, 383
- Antonucci R., 1993, *ARA&A*, 31, 473
- Astropy Collaboration, 2013, *A&A*, 558, A33
- Astropy Collaboration, 2018, *AJ*, 156, 123
- Becker R. H., White R. L., Helfand D. J., 1995, *ApJ*, 450, 559
- Boroson T. A., Green R. F., 1992, *ApJS*, 80, 109
- Buttiglione S., Capetti A., Celotti A., Axon D. J., Chiaberge M., Macchetto F. D., Sparks W. B., 2009, *A&A*, 495, 1033
- Cackett E. M., Chiang C.-Y., McHardy I., Edelson R., Goad M. R., Horne K., Korista K. T., 2018, *ApJ*, 857, 53
- Capellupo D. M., Netzer H., Lira P., Trakhtenbrot B., Mejía-Restrepo J., 2015, *MNRAS*, 446, 3427
- Capellupo D. M., Netzer H., Lira P., Trakhtenbrot B., Mejía-Restrepo J., 2016, *MNRAS*, 460, 212
- Cardelli J. A., Clayton G. C., Mathis J. S., 1989, *ApJ*, 345, 245
- Chakravorty S., Kembhavi A. K., Elvis M., Ferland G., 2009, *MNRAS*, 393, 83
- Coleman M. S. B., Blaes O., Hirose S., Hauschildt P. H., 2018, *ApJ*, 857, 52

¹<http://www.astropy.org>

- Coleman M. S. B., Kotko I., Blaes O., Lasota J. P., Hirose S., 2016, *MNRAS*, 462, 3710
- Collinson J. S., Ward M. J., Landt H., Done C., Elvis M., McDowell J. C., 2017, *MNRAS*, 465, 358
- Condon J. J., Cotton W. D., Greisen E. W., Yin Q. F., Perley R. A., Taylor G. B., Broderick J. J., 1998, *AJ*, 115, 1693
- Davis S. W., Woo J.-H., Blaes O. M., 2007, *ApJ*, 668, 682
- Done C., Davis S. W., Jin C., Blaes O., Ward M., 2012, *MNRAS*, 420, 1848 (D12)
- Done C., Gierliński M., Kubota A., 2007, *A&AR*, 15, 1
- Fanidakis N., Baugh C. M., Benson A. J., Bower R. G., Cole S., Done C., Frenk C. S., 2011, *MNRAS*, 410, 53
- Fawcett V. A., Alexander D. M., Rosario D. J., Klindt L., Lusso E., Morabito L. K., Rivera G. C., 2022, *MNRAS*, 513, 1254
- Foschini L. et al., 2012, *A&A*, 548, A106
- Gierliński M., Done C., 2004, *MNRAS*, 349, L7
- Gravity Collaboration, 2018, *Nature*, 563, 657
- Greene J. E. et al., 2010, *ApJ*, 723, 409
- Griffin A. J., Lacey C. G., Gonzalez-Perez V., Lagos C. d. P., Baugh C. M., Fanidakis N., 2019, *MNRAS*, 487, 198
- Guo H., Liu X., Shen Y., Loeb A., Monroe T., Prochaska J. X., 2019, *MNRAS*, 482, 3288
- Guo H., Shen Y., Wang S., 2018, PyQSOFit: Python Code to Fit the Spectrum of Quasars, Available at: <https://ui.adsabs.harvard.edu/abs/2018ascl.soft09008G>.
- Haardt F., Maraschi L., 1991, *ApJ*, 380, L51
- Haardt F., Maraschi L., 1993, *ApJ*, 413, 507
- Hagen S., Done C., 2023, preprint ([arXiv:2304.01253](https://arxiv.org/abs/2304.01253))
- Hao H. et al., 2010, *ApJ*, 724, L59
- Hubeny I., Blaes O., Krolik J. H., Agol E., 2001, *ApJ*, 559, 680
- Huško F., Lacey C. G., Schaye J., Schaller M., Nobels F. S. J., 2022, *MNRAS*, 516, 3750
- Jiang Y.-F., Blaes O., 2020, *ApJ*, 900, 25
- Jiang Y.-F., Cantiello M., Bildsten L., Quataert E., Blaes O., 2015, *ApJ*, 813, 74
- Jiang Y.-F., Davis S. W., Stone J. M., 2016a, *ApJ*, 827, 10
- Jiang Y.-F., Guillochon J., Loeb A., 2016b, *ApJ*, 830, 125
- Jin C., Ward M., Done C., Gelbord J., 2012, *MNRAS*, 420, 1825
- Kastra J. S. et al., 2014, *Science*, 345, 64
- Kellermann K. I., Sramek R., Schmidt M., Shaffer D. B., Green R., 1989, *AJ*, 98, 1195
- Korista K. T., Goad M. R., 2001, *ApJ*, 553, 695
- Korista K. T., Goad M. R., 2019, *MNRAS*, 489, 5284
- Krumpe M. et al., 2017, *A&A*, 607, L9
- Kubota A., Done C., 2018, *MNRAS*, 480, 1247 (KD18)
- Kubota A., Done C., 2019, *MNRAS*, 489, 524
- Kynoch D., Mitchell J. A. J., Ward M. J., Done C., Lusso E., Landt H., 2023, *MNRAS*, 520, 2781 (K23)
- Landt H. et al., 2023, *ApJ*, 945, 62
- Laor A., Davis S. W., 2014, *MNRAS*, 438, 3024
- Laor A., Netzer H., 1989, *MNRAS*, 238, 897
- Lawrence A., 2012, *MNRAS*, 423, 451
- Lawrence A., 2018, *Nat. Astron.*, 2, 102
- Lu Y., Wang T., Zhou H., Wu J., 2007, *AJ*, 133, 1615
- Lusso E. et al., 2010, *A&A*, 512, A34
- Lusso E., Fumagalli M., Rafelski M., Neeleman M., Prochaska J. X., Hennawi J. F., O'Meara J. M., Theuns T., 2018, *ApJ*, 860, 41
- Lusso E., Risaliti G., 2016a, *ApJ*, 819, 154
- Lusso E., Risaliti G., 2016b, *ApJ*, 819, 154
- Malzac J., Belloni T., Spruit H. C., Kanbach G., 2003, *A&A*, 407, 335
- Mejía-Restrepo J. E., Trakhtenbrot B., Lira P., Netzer H., Capellupo D. M., 2016, *MNRAS*, 460, 187
- Miniutti G. et al., 2014, *MNRAS*, 437, 1776
- Narayan R., Yi I., 1995, *ApJ*, 452, 710
- Noda H., Done C., 2018, *MNRAS*, 480, 3898
- Novikov I. D., Thorne K. S., 1973, in *Black Holes (Les Astres Occlus)*. Gordon and Breach, Paris, p. 343
- Page M. J. et al., 2012, *MNRAS*, 426, 903
- Pàris I. et al., 2018, *A&A*, 613, A51
- Petrucci P. O., Ursini F., De Rosa A., Bianchi S., Cappi M., Matt G., Dadina M., Malzac J., 2018, *A&A*, 611, A59
- Porquet D., Reeves J. N., O'Brien P., Brinkmann W., 2004, *A&A*, 422, 85
- Rakshit S., Stalin C. S., Chand H., Zhang X.-G., 2017, *ApJS*, 229, 39 (R17)
- Rakshit S., Stalin C. S., Kotilainen J., 2020, *ApJS*, 249, 17 (R20)
- Reichard T. A. et al., 2003, *AJ*, 126, 2594
- Reynolds C. S., Fabian A. C., 1995, *MNRAS*, 273, 1167
- Ro S., 2019, *ApJ*, 873, 76
- Ruan J. J., Anderson S. F., Eracleous M., Green P. J., Haggard D., MacLeod C. L., Runnoe J. C., Sobolewska M. A., 2019, *ApJ*, 883, 76
- Schlafly E. F., Finkbeiner D. P., 2011, *ApJ*, 737, 103
- Shakura N. I., Sunyaev R. A., 1973, *A&A*, 24, 337
- Shen Y. et al., 2019, *ApJS*, 241, 34
- Stern B. E., Poutanen J., Svensson R., Sikora M., Begelman M. C., 1995, *ApJ*, 449, L13
- Temple M. J. et al. 2023, *MNRAS*, 523, 646
- Torrealba J., Chavushyan V., Cruz-González I., Arshakian T. G., Bertone E., Rosa-González D., 2012, *RMxAA*, 48, 9
- Vasudevan R. V., Fabian A. C., 2007, *MNRAS*, 381, 1235
- Vasudevan R., 2008, The Effective Eddington Limit for AGN, XMM-Newton Proposal ID 06050903
- Volonteri M., Sikora M., Lasota J.-P., 2007, *ApJ*, 667, 704
- Webb N. A. et al., 2020, *A&A*, 000, 0
- Woo J.-H., Le H. A. N., Karouzos M., Park D., Park D., Malkan M. A., Treu T., Bennert V. N., 2018, *ApJ*, 859, 138

APPENDIX A: THE SOUX SAMPLE CHANGING MASS AT FIXED LUMINOSITY

Fig. A1 shows the changing mass spectra for each luminosity bin covered by the SOUX sample for any L_{3000} bin spanning more than three mass bins. The broad line profiles clearly broaden with increasing mass.

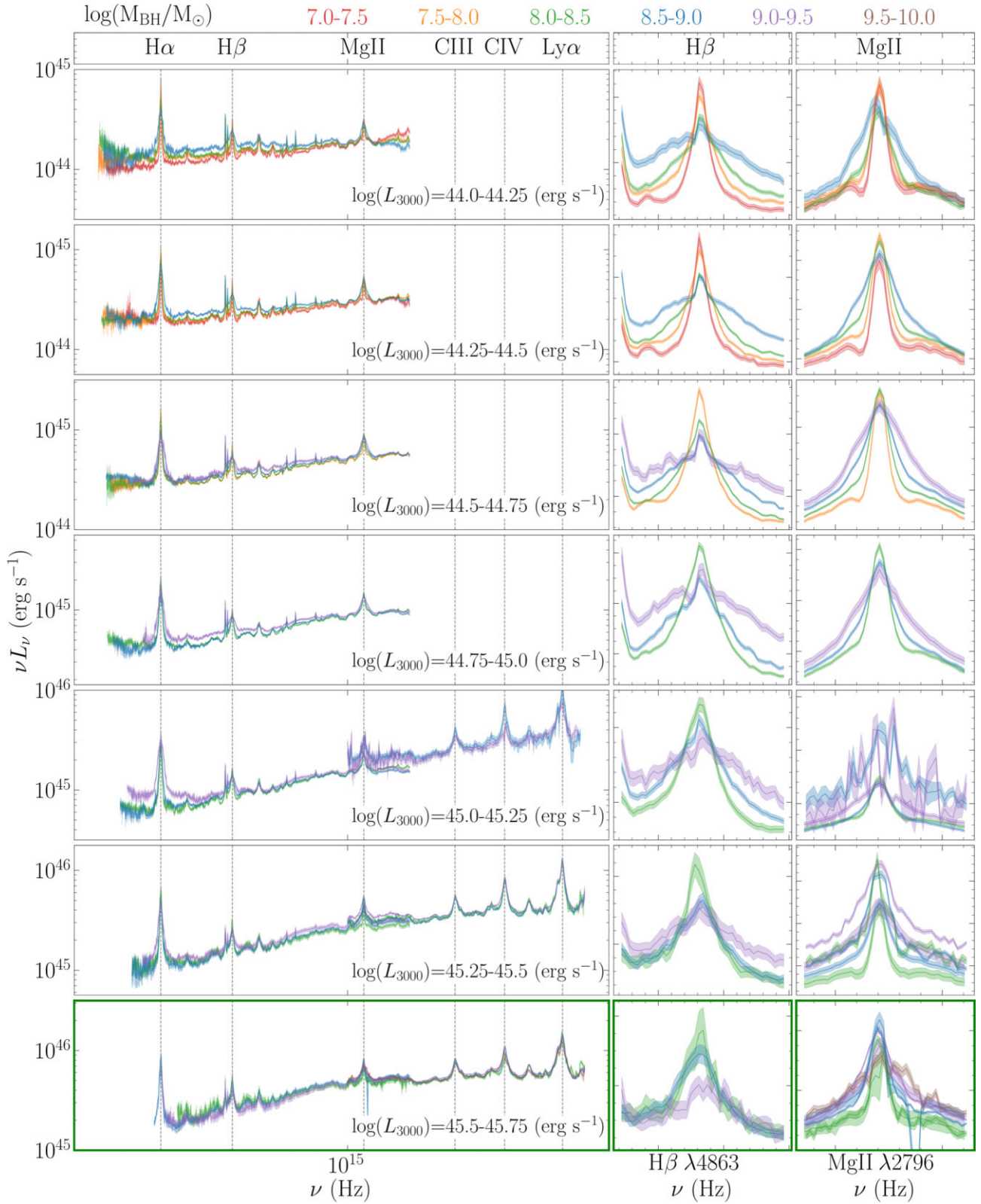


Figure A1. All luminosity bins shown in Fig. 9 that span more than 3 populated mass bins over plotted, showing the unchanging spectral shapes across the mass ranges. The right-hand panels show the H β and Mg II emission line regions. A separate Mg II profile is for shown for both the low and the high z composite in any L_{3000} with overlap.

APPENDIX B: THE WIDER SDSS PARAMETER SPACE

Here, we present composite spectra for the entire SDSS parameter space with $z \leq 0.8$ or $2.0 \leq z \leq 2.15$.

Fig. B1 shows the composite spectrum corresponding to each M_{BH} , L_{3000} gridpoint coloured by the number of sources in each bin. The gridpoints populated by the SOUX AGN sample inhabit the centre of

and the most highly populated section of the parameter space. This is expected as the SOUX AGN sample is comprised of sources with high quality data *XMM-Newton* data which are relatively rare and therefore more likely to be found in the more highly populated bins.

Fig. B2 shows the same bins and composites as Fig. B1 but coloured with the resultant $\log(\dot{m})$ value from the fitting of QSOSED to a 500 Å window of constant flux set at the central L_{3000} value for each respective bin.

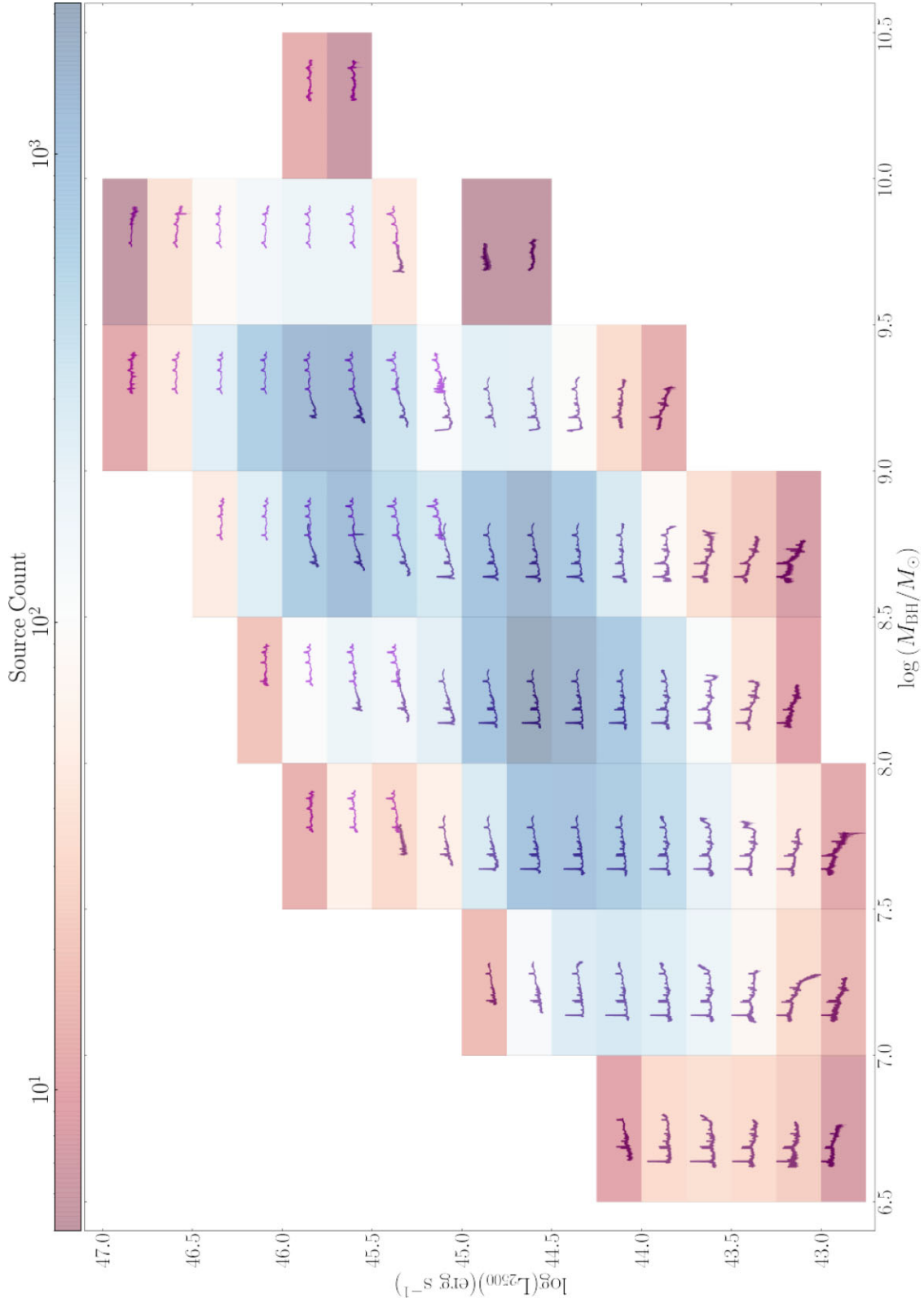


Figure B1. SDSS composites for the entire parameter space $\log(M_{\text{BH}}/M_{\odot})$ and $\log(L_{2500})$ (erg s^{-1}). Each bin is coloured by the number of sources contained within.

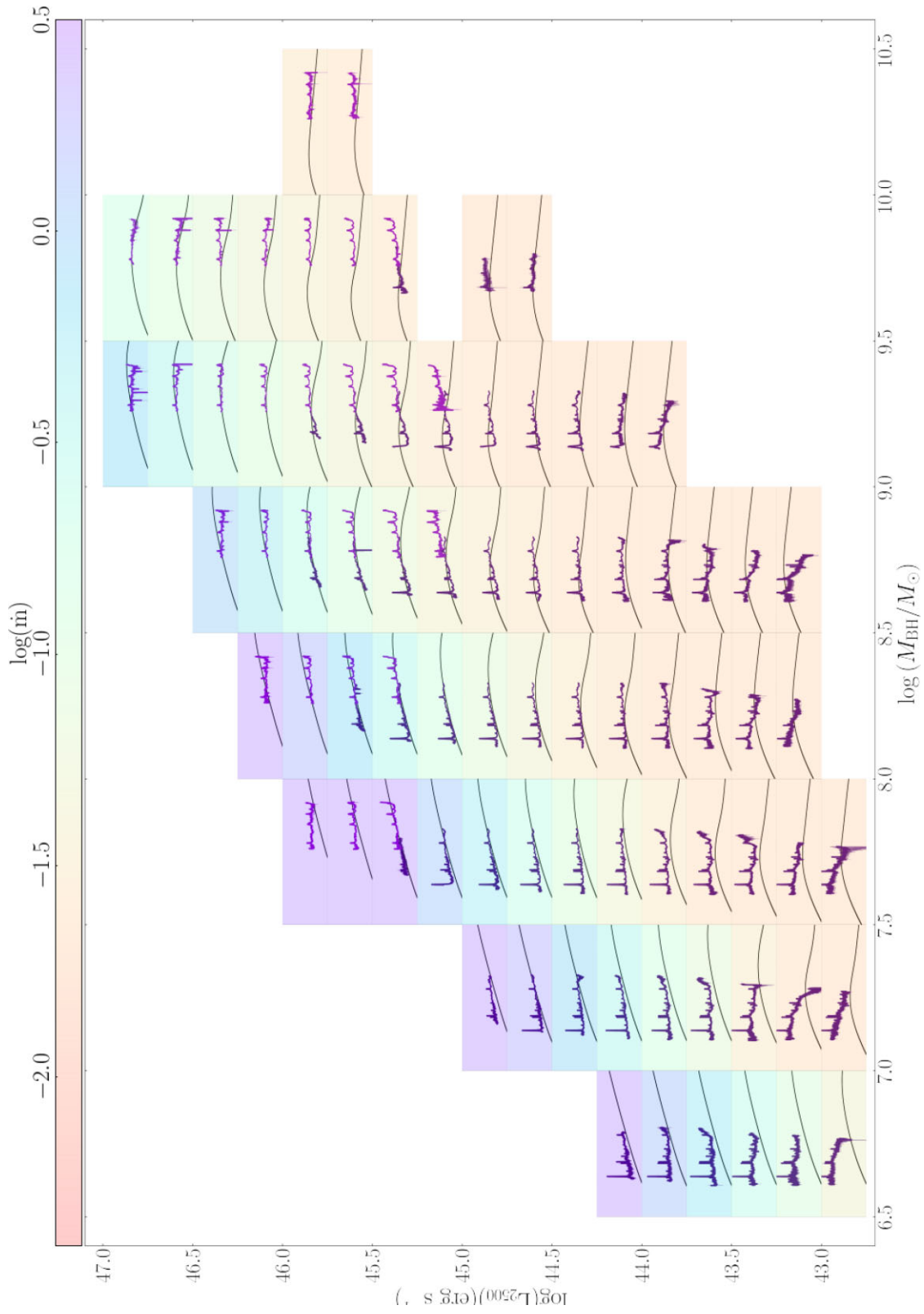


Figure B2. SDSS composites for the entire parameter space $\log(M_{\text{BH}}/M_{\odot}) = (6.5-10.5)$ and $\log(L_{3000}) = (42.75-47.0)$ erg s^{-1} . A QSOSED model has been fit to a 500 \AA wide bandpass of the central L_{3000} luminosity for each bin. Each bin is coloured with the resultant z_i values.

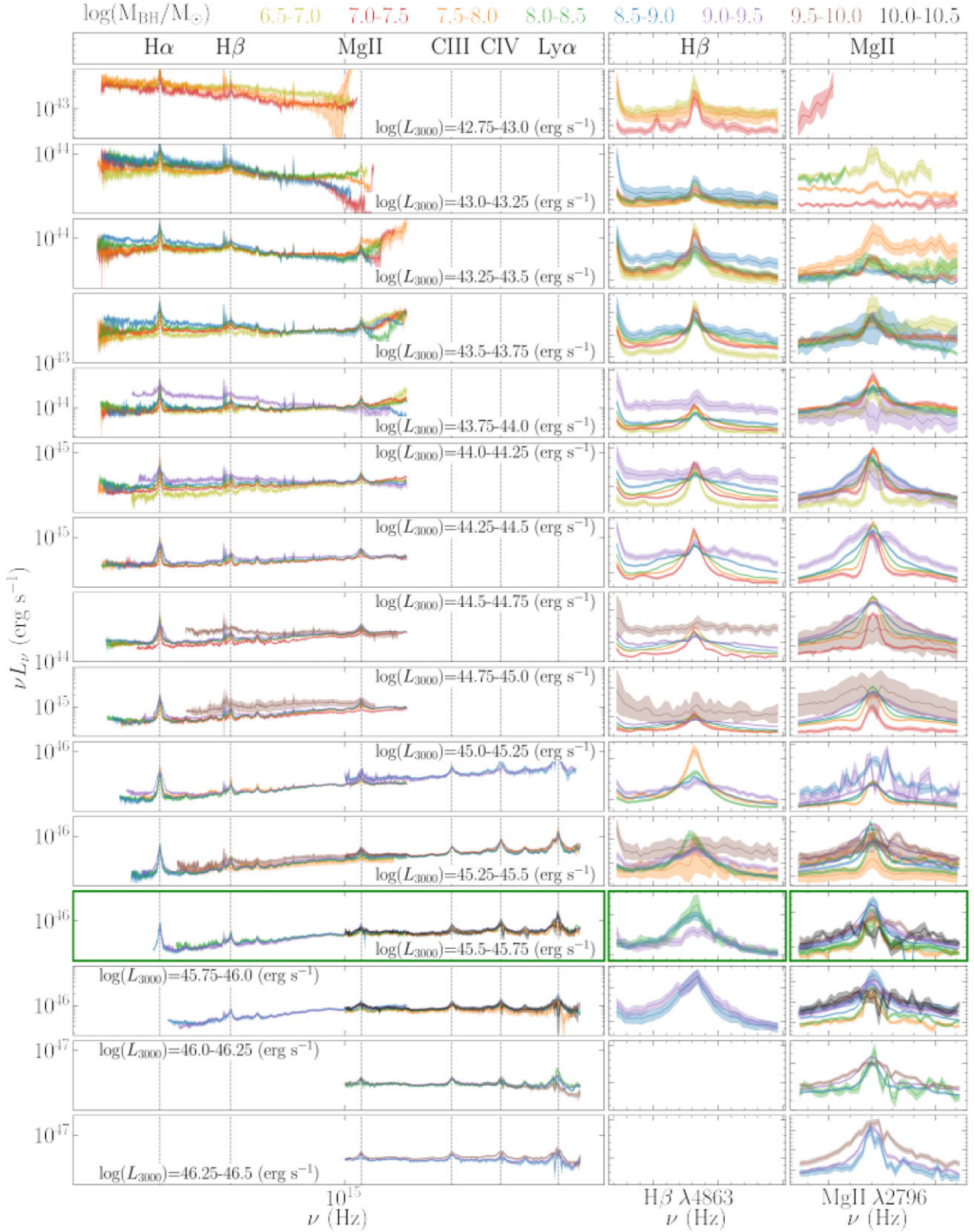


Figure B3. All luminosity bins shown in Fig. B2 that span more than three populated mass bins over plotted, showing the unchanging spectral shapes across the mass ranges.

APPENDIX C: X-SHOOTER SPECTRAL COMPARISON

We take a sample of sources from Capellupo et al. (2015) and Fawcett et al. (2022) observed with X-shooter, to compare our results with a wider sample of AGN, not observed with SDSS. These spectra were obtained through private communication. The X-shooter spectra defined as the control sample in Fawcett et al. (2022), were separated into the L_{3000} bins shown in Fig. B3. A geometric composite was created for any mass-luminosity bin containing more than one source and individual spectra considered for bins only containing one object, these spectra are shown in Fig. C1.

The spectral shape of the X-shooter data spanning 1.5 dex in mass, are well matched across all luminosity bins to the shape of the SDSS composites displayed in Fig. B3 and plotted in grey in Fig. C1.

The X-shooter sample display no significant change in spectral shape with changing mass when compared to the SDSS spectra. The central panel of Fig. C1 representing the $\log(L_{3000}) = 45.5 - 45.75$ (erg s^{-1}) bin, shows three X-shooter spectra spanning 1.5 dex in mass between 8.5 and 10.0 $\log(M_{\text{BH}}/M_{\odot})$. These three spectra do not show any significant change in spectral shape.

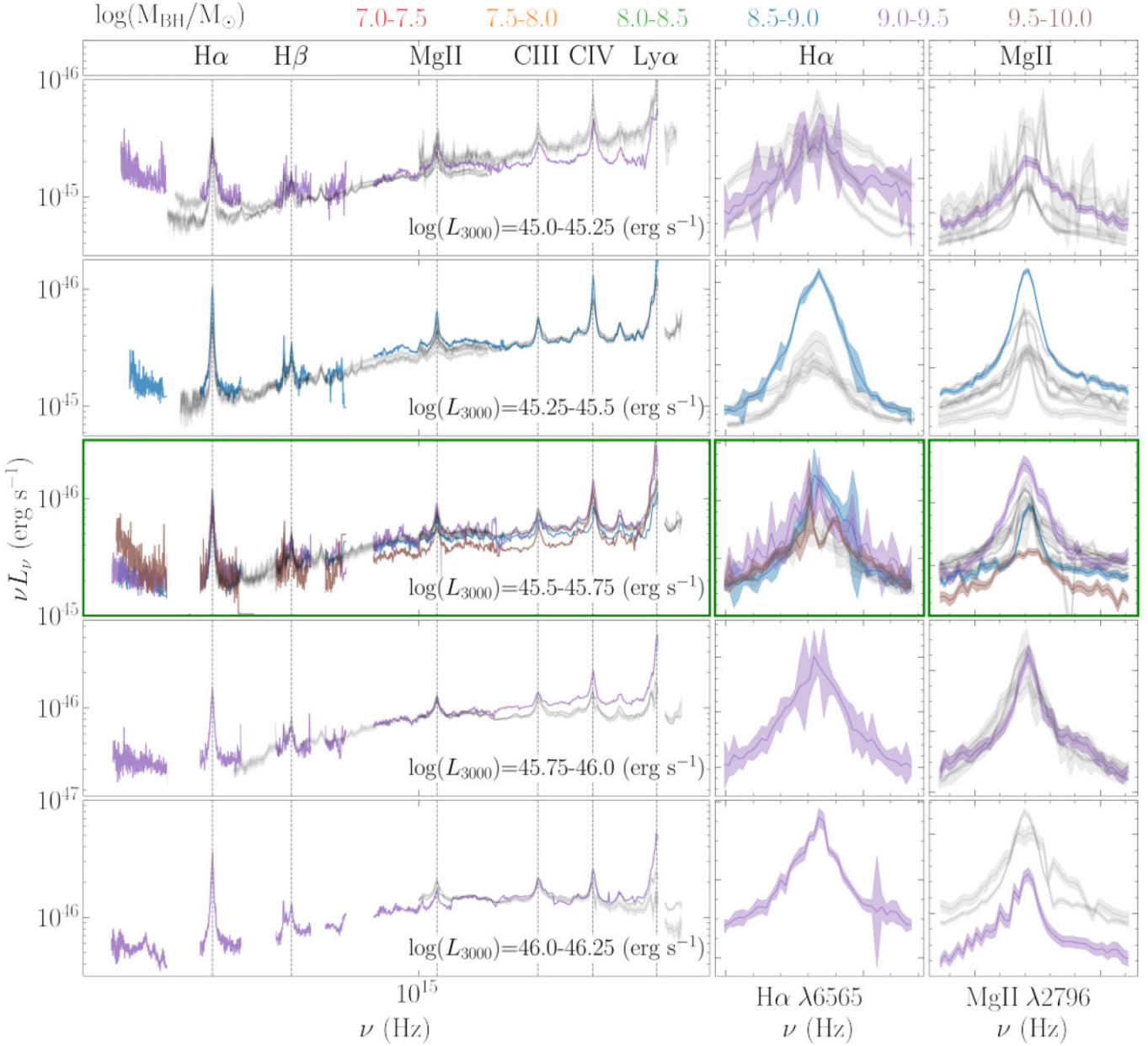


Figure C1. Four L_{3000} bins with the SDSS data from Fig. B3 plotted in grey. Composite or individual X-shooter spectra taken from Capellupo et al. (2015) and Fawcett et al. (2022) are overplotted and coloured by mass.

APPENDIX D: SOURCES REMOVED FROM SOUX AGN SAMPLE

We performed a visual inspection on the *XMM-Newton* UV and X-ray data for each source and removed any object displaying a spectral

shape indicative of intrinsic absorption. In Table D1, we list all of the 54 sources that were removed before the fitting procedure.

Table D1. Sources removed upon visual inspection due to evidence of intrinsic absorption in the *XMM-Newton* data. Columns: (1) SDSS-ID composed of PLATE, MJD, and FIBREID from R20, (2) Right Ascension, (3) Declination, (4) Redshift as quoted by R20, and (5) Mass as calculated in K23 using the scaling relations from (Mejía-Restrepo et al. 2016).

SDSS-ID	Right Ascension	Declination	Redshift	Mass (M_{\odot})
0391-51782-0360	00 22 09.9	+ 00 16 29.3	0.57	1.74E + 08
0412-52258-0400	03 06 39.5	+ 00 03 43.1	0.11	2.60E + 07
0422-51811-0224	01 07 12.0	+ 14 08 44.9	0.08	2.44E + 06
0514-51994-0331	11 40 08.7	+ 03 07 11.4	0.08	3.19E + 06
0539-52017-0171	15 01 48.8	+ 01 44 05.1	0.48	4.93E + 07
0552-51992-0440	09 02 31.2	+ 52 07 49.6	0.13	8.76E + 06
0616-52374-0442	15 36 41.6	+ 54 35 05.5	0.45	1.86E + 08
0623-52051-0257	16 12 32.4	+ 51 24 01.3	0.36	7.89E + 08
0629-52051-0200	16 42 51.3	+ 44 15 01.3	1.15	2.92E + 09
0639-52146-0179	21 18 52.9	-07 32 27.5	0.26	2.57E + 07
0709-52205-0040	03 07 07.4	-00 04 24.0	0.66	8.29E + 07
1266-52709-0205	08 13 03.8	+ 25 42 11.0	2.02	1.64E + 09
1365-53062-0378	11 17 06.3	+ 44 13 33.3	0.14	4.72E + 08
1423-53167-0603	16 44 42.5	+ 26 19 13.2	0.14	1.43E + 07
1604-53078-0566	11 13 54.6	+ 12 44 39.0	0.68	4.50E + 07
1643-53143-0172	14 14 49.5	+ 36 12 40.2	0.18	3.89E + 06
1744-53055-0630	10 07 26.0	+ 12 48 56.2	0.24	2.62E + 09
1745-53061-0309	10 07 54.9	+ 12 18 42.1	0.76	2.28E + 08
1795-54507-0457	13 09 46.9	+ 08 19 48.2	0.15	3.22E + 08
1978-53473-0039	13 38 07.4	+ 28 05 09.8	1.09	5.38E + 08
1994-53845-0267	12 53 17.5	+ 31 05 50.6	0.78	8.09E + 08
2016-53799-0061	13 12 17.7	+ 35 15 21.0	0.18	8.98E + 08
2020-53431-0051	12 42 10.6	+ 33 17 02.6	0.04	1.28E + 07
2123-53793-0443	14 07 00.3	+ 28 27 14.6	0.08	5.04E + 08
2132-53493-0349	14 23 15.5	+ 23 58 17.5	0.44	1.03E + 09
2288-53699-0617	09 18 48.6	+ 21 17 17.0	0.15	1.96E + 07
2289-53708-0130	09 25 54.7	+ 19 54 05.1	0.19	1.78E + 09
2434-53826-0093	09 07 59.3	+ 13 51 35.0	0.45	2.49E + 08
2501-54084-0384	11 27 36.9	+ 24 49 23.4	0.06	6.85E + 06
2511-53882-0555	11 49 15.4	+ 23 12 33.6	1.06	9.22E + 08
2763-54507-0581	14 53 01.4	+ 16 44 52.6	0.84	5.08E + 09
2784-54529-0010	14 06 21.8	+ 22 23 46.5	0.1	1.38E + 07
3936-55302-0730	15 50 14.8	+ 21 24 31.4	0.48	6.34E + 07
4388-55536-0940	02 33 31.0	-05 45 50.9	0.49	1.47E + 09
4558-55569-0008	10 34 16.2	+ 39 32 40.8	1.41	3.30E + 09
4773-55648-0076	10 45 19.8	+ 04 19 51.2	0.8	7.41E + 08
4832-55680-0150	12 19 32.3	+ 05 40 05.2	1.11	2.56E + 09
5333-56001-0534	10 07 51.1	+ 12 45 26.4	0.21	2.73E + 06
5365-55945-0380	11 12 38.0	+ 13 22 44.9	0.43	1.33E + 08
5423-55958-0636	13 09 36.2	+ 08 28 15.3	0.78	1.19E + 09
6370-56238-0807	02 29 29.4	+ 00 34 41.1	1.25	2.84E + 08
6404-56330-0249	11 55 35.8	+ 23 27 23.1	0.14	6.55E + 07
6404-56330-0294	11 55 04.1	+ 23 31 17.9	1.08	7.20E + 08
6676-56389-0806	12 11 46.2	+ 50 31 04.6	1.16	7.76E + 08
6723-56428-0410	15 45 55.5	+ 48 49 29.8	0.15	1.31E + 07
6732-56370-0806	14 48 55.6	+ 48 30 14.4	0.68	2.20E + 08
7235-56603-0274	02 29 28.4	-05 11 25.0	0.31	2.39E + 07
7235-56603-0293	02 29 17.1	-05 29 01.4	0.19	9.13E + 07
7299-56686-0377	09 47 04.5	+ 47 21 42.9	0.54	9.06E + 07
7339-56772-0577	14 07 59.0	+ 53 47 59.7	0.17	9.50E + 07
7419-56811-0620	12 34 13.3	+ 47 53 51.1	0.37	2.09E + 08
7578-56956-0312	22 18 11.2	+ 19 30 39.8	1.28	3.99E + 09
7841-56960-0809	01 58 46.0	-01 49 40.5	0.51	6.64E + 08
7877-56898-0913	01 25 39.4	-01 13 08.4	1.08	2.98E + 08

This paper has been typeset from a $\text{\TeX}/\text{\LaTeX}$ file prepared by the author.